



Calhoun: The NPS Institutional Archive
DSpace Repository

Theses and Dissertations

1. Thesis and Dissertation Collection, all items

2014-12

Impact of convection on surface fluxes observed during LASP/DYNAMO 2011

Cushanick, Matthew S.

Monterey, California. Naval Postgraduate School

<http://hdl.handle.net/10945/44544>

This publication is a work of the U.S. Government as defined in Title 17, United States Code, Section 101. Copyright protection is not available for this work in the United States.

Downloaded from NPS Archive: Calhoun



<http://www.nps.edu/library>

Calhoun is the Naval Postgraduate School's public access digital repository for research materials and institutional publications created by the NPS community. Calhoun is named for Professor of Mathematics Guy K. Calhoun, NPS's first appointed -- and published -- scholarly author.

Dudley Knox Library / Naval Postgraduate School
411 Dyer Road / 1 University Circle
Monterey, California USA 93943



NAVAL POSTGRADUATE SCHOOL

MONTEREY, CALIFORNIA

THESIS

**IMPACT OF CONVECTION ON SURFACE FLUXES
OBSERVED DURING LASP/DYNAMO 2011**

by

Matthew S. Cushmanick

December 2014

Thesis Advisor:
Second Reader:

Qing Wang
Wendell Nuss

Approved for public release; distribution is unlimited

THIS PAGE INTENTIONALLY LEFT BLANK

REPORT DOCUMENTATION PAGE			Form Approved OMB No. 0704-0188	
Public reporting burden for this collection of information is estimated to average 1 hour per response, including the time for reviewing instruction, searching existing data sources, gathering and maintaining the data needed, and completing and reviewing the collection of information. Send comments regarding this burden estimate or any other aspect of this collection of information, including suggestions for reducing this burden, to Washington headquarters Services, Directorate for Information Operations and Reports, 1215 Jefferson Davis Highway, Suite 1204, Arlington, VA 22202-4302, and to the Office of Management and Budget, Paperwork Reduction Project (0704-0188) Washington, DC 20503.				
1. AGENCY USE ONLY (Leave blank)		2. REPORT DATE December 2014		3. REPORT TYPE AND DATES COVERED Master's Thesis
4. TITLE AND SUBTITLE IMPACT OF CONVECTION ON SURFACE FLUXES OBSERVED DURING LASP/DYNAMO 2011			5. FUNDING NUMBERS	
6. AUTHOR(S) Matthew S. Cushmanick				
7. PERFORMING ORGANIZATION NAME(S) AND ADDRESS(ES) Naval Postgraduate School Monterey, CA 93943-5000			8. PERFORMING ORGANIZATION REPORT NUMBER	
9. SPONSORING /MONITORING AGENCY NAME(S) AND ADDRESS(ES) N/A			10. SPONSORING/MONITORING AGENCY REPORT NUMBER	
11. SUPPLEMENTARY NOTES The views expressed in this thesis are those of the author and do not reflect the official policy or position of the Department of Defense or the U.S. Government. IRB protocol number ____ N/A ____.				
12a. DISTRIBUTION / AVAILABILITY STATEMENT Approved for public release; distribution is unlimited			12b. DISTRIBUTION CODE A	
13. ABSTRACT (maximum 200 words) The NOAA WP-3D aircraft made extensive measurements over the tropical Indian Ocean during the Littoral Air-Sea Processes (LASP)/Dynamics of Madden-Julian Oscillation (DYNAMO) experiment. The low-level measurements from the WP-3D are analyzed here to examine the impact of tropical convection and its associated cold pool in modifying surface exchange of momentum and energy. Analysis of surface fluxes under convection and non-convection demonstrates the increased variability of surface fluxes under convection. Fluxes below convection are larger in magnitude, variable, and demonstrate no clear contribution from specific length scales. The lack of clear transport in the turbulence scales under convection highlights that additional processes beyond turbulence transport are occurring, which points to the role of precipitation evaporation below the cloud base. In contrast, surface fluxes under non-convective conditions are smaller and have a clear positive contribution throughout the turbulence region. Comparison of eddy correlation method with the COARE bulk surface flux parameterization indicates large scattering for the convective cases. Stress and latent heat flux from the COARE algorithm show good comparison with the eddy correlation fluxes, while the sensible heat flux seem to be consistently over-predicted, which may be a result of uncertainties in the measured sea surface temperature.				
14. SUBJECT TERMS LASP/DYNAMO 2011, aircraft measurement, turbulent flux, surface flux, surface layer, eddy correlation method, COARE bulk surface flux parameterization, cold pool, convection, precipitation			15. NUMBER OF PAGES 85	
			16. PRICE CODE	
17. SECURITY CLASSIFICATION OF REPORT Unclassified	18. SECURITY CLASSIFICATION OF THIS PAGE Unclassified	19. SECURITY CLASSIFICATION OF ABSTRACT Unclassified	20. LIMITATION OF ABSTRACT UU	

THIS PAGE INTENTIONALLY LEFT BLANK

Approved for public release; distribution is unlimited

**IMPACT OF CONVECTION ON SURFACE FLUXES OBSERVED DURING
LASP/DYNAMO 2011**

Matthew S. Cushmanick
Lieutenant Commander, United States Navy
B.S., United States Naval Academy, 2004
M.S., Naval Postgraduate School, 2005

Submitted in partial fulfillment of the
requirements for the degree of

**MASTER OF SCIENCE IN METEOROLOGY AND PHYSICAL
OCEANOGRAPHY**

from the

**NAVAL POSTGRADUATE SCHOOL
December 2014**

Author: Matthew S. Cushmanick

Approved by: Qing Wang, Ph.D.
Thesis Advisor

Wendell Nuss, Ph.D.
Second Reader

Wendell Nuss, Ph.D.
Chair, Department of Meteorology

THIS PAGE INTENTIONALLY LEFT BLANK

ABSTRACT

The NOAA WP-3D aircraft made extensive measurements over the tropical Indian Ocean during the Littoral Air-Sea Processes (LASP)/Dynamics of Madden-Julian Oscillation (DYNAMO) experiment. The low-level measurements from the WP-3D are analyzed here to examine the impact of tropical convection and its associated cold pool in modifying surface exchange of momentum and energy. Analysis of surface fluxes under convection and non-convection demonstrates the increased variability of surface fluxes under convection. Fluxes below convection are larger in magnitude, variable, and demonstrate no clear contribution from specific length scales. The lack of clear transport in the turbulence scales under convection highlights that additional processes beyond turbulence transport are occurring, which points to the role of precipitation evaporation below the cloud base. In contrast, surface fluxes under non-convective conditions are smaller and have a clear positive contribution throughout the turbulence region.

Comparison of eddy correlation method with the COARE bulk surface flux parameterization indicates large scattering for the convective cases. Stress and latent heat flux from the COARE algorithm show good comparison with the eddy correlation fluxes, while the sensible heat flux seem to be consistently over-predicted, which may be a result of uncertainties in the measured sea surface temperature.

THIS PAGE INTENTIONALLY LEFT BLANK

TABLE OF CONTENTS

I.	INTRODUCTION.....	1
A.	SURFACE FLUXES AND FORECAST ACCURACY	1
B.	SURFACE FLUXES AND MILITARY OPERATIONS.....	2
C.	THESIS OBJECTIVES.....	3
II.	BACKGROUND.....	5
A.	TURBULENT FLUXES	5
B.	PARAMETERIZATION FOR FORECAST MODELING	6
C.	UNCERTAINTIES IN SURFACE FLUXES AND THEIR PARAMETERIZATION	7
D.	CONVECTIVE COLD POOLS AND SURFACE FLUXES	10
E.	MADDEN-JULIAN OSCILLATION AND TROPICAL CONVECTION	14
III.	AIRCRAFT MEASUREMENTS IN LASP/DYNAMO	17
A.	OVERVIEW	17
B.	DATA COLLECTION MODULES AND VARIABLES.....	19
C.	SUMMARY OF FLIGHT CONDITIONS AND LOW LEVEL LEGS FOR EACH FLIGHT	22
IV.	DATA ANALYSIS METHODS AND RESULTS.....	27
A.	DEFINING LEVEL LEGS	27
B.	SEA SURFACE TEMPERATURE CORRECTION.....	29
C.	SEPARATION OF CONVECTION AND NON-CONVECTION REGIONS.....	31
D.	CALCULATING TURBULENT FLUXES.....	32
E.	OVERALL COMPARISON OF TURBULENT FLUXES.....	33
F.	CHARACTERISTICS OF TURBULENT FLUXES	36
G.	SPECTRAL CHARACTERISTICS OF TURBULENCE	42
H.	VERTICAL VARIATION OF TURBULENCE	50
I.	EVALUATION OF COARE BULK SURFACE FLUX PARAMETERIZATION	52
V.	CONCLUSIONS.....	57
A.	SUMMARY AND CONCLUSIONS.....	57
B.	REMAINING ISSUES AND RECOMMENDATIONS.....	59
	LIST OF REFERENCES.....	61
	INITIAL DISTRIBUTION LIST	65

THIS PAGE INTENTIONALLY LEFT BLANK

LIST OF FIGURES

Figure 1.	Time series of in-situ data collected during the penetration of a gust front (from Jorgensen et al. 1997).	11
Figure 2.	Comparison of specific humidity and potential temperature in undisturbed (solid), highly disturbed (dash), and recovering (dash-dot) boundary layers at the indicated distances to the leading edge of a convective gust front (from Jorgensen et al. 1997).	12
Figure 3.	Schematic of cold pool development and spreading under deep convection (from Tompkins 2001).	13
Figure 4.	Schematics of the MJO convective region and its eastward development (from Zhang 2005).	16
Figure 5.	NOAA Lockheed WP-3D Orion (from NOAA Air Operations Center 2014).	17
Figure 6.	DYNAMO operations area.	19
Figure 7.	FVS maneuver used in the LASP/DYNAMO experiment (from Wang et al. 2013).	20
Figure 8.	FFM maneuver used in the LASP/DYNAMO experiment (from Wang et al. 2013).	21
Figure 9.	RF02 P-3 flight track (blue) on November 13, 2011.	23
Figure 10.	Aircraft altitude and heading for RF08. Time is in coordinated universal time (UTC).	28
Figure 11.	Aerial view of RF08 flight track (light gray) and all level legs. The altitude of measurement for each LL is indicated by the color bar.	28
Figure 12.	Comparison of colocated aircraft radiometric SST with AXBT/AXCTD top water temperature from LASP/DYNAMO (courtesy of Dr. Denny Alappattu).	30
Figure 13.	Visible satellite imagery on 0900 UTC, November 22, 2011 (RF05). The convective region is identified as the area covered by deep convective clouds (after Wang et al. 2013).	32
Figure 14.	Low level turbulent fluxes from eddy correlation method for all flights for (a) LHF, (b) SHF, and (c) stress. Red points represent convective cases and blue points represent non-convective cases. ..	34
Figure 15.	Boxplots of LHF calculated by eddy correlation method for each flight. Phases of Madden-Julian oscillation are separated by vertical lines. Convective cases are in red and non-convective cases are in blue.	35
Figure 16.	Same as in Figure 15, except for SHF.	36
Figure 17.	Same as in Figure 15, except for stress.	36
Figure 18.	Latent heat flux (LHF) variation with height for (a) non-convective cases and (b) convective cases. The legend links data points with their corresponding research flight number. The dashed line is illustrative of the flux gradient in LHF.	38
Figure 19.	Same as Figure 18, except for SHF.	38

Figure 20.	Same as Figure 18, except for stress.	38
Figure 21.	Variability of LHF with ASTD while (a) not under convection and (b) under convection. The legend shows the corresponding flight numbers.	40
Figure 22.	Same as Figure 21, except for SHF.	40
Figure 23.	Same as Figure 21, except for stress.	40
Figure 24.	Variation of LHF with mean wind speed while (a) not under convection and (b) under convection.	41
Figure 25.	Same as Figure 24, except for SHF.	42
Figure 26.	Same as Figure 24, except for stress.	42
Figure 27.	Time series of latent heat flux, sensible heat flux, and stress for RF08 LL1. First half of the LL is under convection and second half of the LL is not. The green dashed boxes define three special data segments (S1, S2, S3) to be discussed later in this section. Time is in UTC.	43
Figure 28.	Time series of several temperature-related variables (see legend), relative humidity, and altitude for RF08 LL1. Regions of convection and non-convection match those in Figure 27. Time is in UTC.	44
Figure 29.	Time series of water vapor, potential temperature, and equivalent potential temperature for RF08 LL1. Regions of convection and non-convection match those in Figure 27. Time is in UTC.	44
Figure 30.	Time series of horizontal (u, v) and vertical (w) component velocities for RF08 LL1. Regions of convection and non-convection match those in Figure 27. Time is in UTC.	45
Figure 31.	Power spectra of vertical velocity of (a) the non-convective segment, and (b) the convective segment of RF08 LL1. The red lines indicate the -5/3 slope for the turbulence inertial subrange.	46
Figure 32.	Same as Figure 31, except for potential temperature.	46
Figure 33.	Same as Figure 31, except for water vapor.	46
Figure 34.	Vertical velocity and water vapor co-spectra of (a) the non-convective segment; and (b) the convective segment of RF08 LL1. ..	47
Figure 35.	Same as Figure 34, except for vertical velocity and potential temperature.	48
Figure 36.	Vertical velocity power spectrum for RF08 LL1 (a) S1, (b) S2, and (c) S3. Red lines indicate the -5/3 slope for the turbulence inertial subrange.	49
Figure 37.	Vertical velocity and water vapor co-spectra for RF08 LL1 (a) S1, (b) S2, and (c) S3.	50
Figure 38.	Same as Figure 38, except for co-spectra of vertical velocity and potential temperature.	50
Figure 39.	Horizontal variation of LHF for all legs of the RF08 FVS. Distances are from a point along the FVS line of bearing to the southwest of all four LL. LL17 is at 60 m, LL18 at 130 m, LL19 at 210 m, and LL20 at 310 m.	51
Figure 40.	Same as Figure 39, except for SHF.	52

Figure 41.	Same as Figure 39, except for stress.	52
Figure 42.	Convective comparison of eddy correlation method flight-measured LHF to COARE bulk surface flux parameterized LHF under (a) non-convective and (b) convective conditions. The dashed line represents a one-to-one comparison.....	54
Figure 43.	Same as Figure 42, except for SHF.	54
Figure 44.	Same as Figure 42, except for stress.	55
Figure 45.	Boxplots comparing eddy correlation method LHF (blue) to COARE bulk surface flux parameterized LHF (red) for (a) not under convection and (b) under convection.....	55
Figure 46.	Same as Figure 45, except for SHF.	56
Figure 47.	Same as Figure 45, except for stress.	56

THIS PAGE INTENTIONALLY LEFT BLANK

LIST OF TABLES

Table 1.	LASP/DYNAMO flight summary (after Wang et al. 2013).....	18
Table 2.	LASP/DYNAMO measured or derived variables used in this study and their sampling rates.	22
Table 3.	Summary of all low LL used in this thesis analysis.....	25

THIS PAGE INTENTIONALLY LEFT BLANK

LIST OF ACRONYMS AND ABBREVIATIONS

AXBT	airborne expendable bathythermograph
AXCTD	airborne expendable conductivity, temperature, and depth
COARE	Coupled Ocean Atmosphere Response Experiment
DYNAMO	Dynamics of Madden-Julian Oscillation
EM	electro-magnetic
EO	electro-optical
FFM	flight-level flux mapping
FVS	flight-level vertical stack
LASP	Littoral Air-Sea Processes
LHF	latent heat flux
LL	level leg
MCS	mesoscale convective systems
MJO	Madden-Julian oscillation
MOST	Monin-Obukhov similarity theory
NOAA	National Oceanic and Atmospheric Administration
RF	research flight
RICO	Rain in Cumulus over the Ocean
R/V	research vessel
SHF	sensible heat flux
SST	sea surface temperature
TOGA	tropical ocean global atmosphere
UTC	coordinated universal time

THIS PAGE INTENTIONALLY LEFT BLANK

ACKNOWLEDGMENTS

Thank you to my thesis advisor, Qing Wang, for her vision on this project. My thesis work would not have been possible without her tireless work ethic and limitless patience. Denny Alappattu was instrumental in the MATLAB coding used in my analysis. I owe him a debt of gratitude for regularly putting aside his work to advance my own. Most of all, thank you to my family for their love and support throughout my graduate education experience at the Naval Postgraduate School.

THIS PAGE INTENTIONALLY LEFT BLANK

I. INTRODUCTION

A. SURFACE FLUXES AND FORECAST ACCURACY

Understanding air-sea fluxes is critical to numerical weather prediction and operational forecasting of the maritime environment, for which proper inclusion of air-sea fluxes is essential because air-sea fluxes characterize the exchange of water vapor, heat, and momentum between the atmosphere and ocean (Kalogiros and Wang 2011). Air-sea fluxes represent the coherent contribution of scalar and vector variables with the individual wind components, their inclusion in any numerical weather prediction model must be parameterized to emulate exchange across the air-sea interface. Emulation is required because the spatial and temporal scales of near surface processes are smaller than the resolution of numerical weather prediction models. Realistic parameterization of air-sea fluxes is crucial because the air-sea interface forms the lower boundary condition within atmospheric modeling and numerical weather prediction schemes. A correct parameterization rests on clearly understanding processes at the air-sea interface under varying conditions. In essence, our ability to diagnose, simulate, and predict the maritime environment rests on our ability to parameterize air-sea fluxes (Fairall et al. 1996b).

Understanding the effects of precipitation and associated convection are additionally important to the parameterization of air-sea fluxes. Application of convection is important because convection couples the planetary boundary layer and free troposphere through the vertical transport of heat, moisture, and momentum (Wang et al. 2009). Convective circulations and their associated precipitation occur at a variety of scales, some of which are too small to be resolved by numerical weather prediction models (Wang and Geerts 2010). When these processes and circulations occur at scales smaller than those resolvable by numerical weather prediction their effects must also be included in the flux parameterization. Due to the mesoscale nature of convective systems, a thorough understanding and comparison of surface exchange processes both

under convection and in its non-convective environment is essential for a model covering an area of $O(\sim 1000 \text{ km})$.

B. SURFACE FLUXES AND MILITARY OPERATIONS

Failure to account for the synoptic and mesoscale evolution of the physical environment will degrade the most detailed operational planning. The physical environment must be accounted for in advance because it is capable of causing mission failure as completely as any enemy force. To improve the chances of mission success, commanders must adjust to environmental conditions to minimize operational cost and maximize unit effectiveness. Understanding the environment within a theater of operations allows the commander to choose suitable windows for operations and protect against losses of manpower and materiel.

While this analysis specifically examines important near surface atmospheric processes within the Indian Ocean, failure to account for atmospheric conditions in any corner of the globe may force units to frequently operate in hazardous or tactically unfavorable conditions. My analysis will specifically focus on the Indian Ocean because of its vital importance to military forces and civilian entities alike as a conduit for maritime shipping and air traffic between Africa, southwest Asia, India, Australia, the Maritime Continent, and the South China Sea. Nevertheless, the results of this study are applicable beyond the Indian Ocean because the processes and parameterization analyzed are utilized globally.

Beyond the general effects of weather conditions, a thorough understanding of surface fluxes is essential at all levels of military planning due to the enormous impacts of convective systems and electro-magnetic/electro-optic (EM/EO) propagation on air and surface military platforms. Ignoring changing surface flux conditions can result in poor numerical weather prediction and inaccurate prediction of EM/EO sensor performance. Poor ability to numerically model and operationally forecast the operating environment may also

result in ineffective or embattled forces due to operations in hazardous weather conditions or tactically unfavorable conditions.

The mission of the military meteorologist is to observe, predict, and advise the commander on current and future impacts to operations. To this end the military meteorologist must be provided the knowledge and numerical weather prediction tools through research to correctly characterize atmospheric processes. This study will work to that end by examining the linkages between surface fluxes and convective processes in a remote region of the world. Improved model surface flux parameterization through analysis could enhance atmospheric model outputs that ultimately attempt to characterize and predict the operational environment. Through better understanding of the environment, the military force achieves a higher probability of mission success by mitigation of the physical environment's negative effects.

C. THESIS OBJECTIVES

This analysis will focus on producing linkages between convection and observed surface fluxes over the Indian Ocean. In-situ sampling of the atmospheric boundary layer was completed on research aircraft during the Littoral Air-Sea Processes (LASP)/Dynamics of Madden-Julian Oscillation (DYNAMO) project. Surface fluxes measured under convective and non-convective conditions will be separated using pre-identified periods of convection over the flight path during each research flight (RF). Using the data available from LASP/DYNAMO, surface fluxes are directly compared during periods with and without convection to ascertain linkages between convective conditions and latent heat flux (LHF), sensible heat flux (SHF), and momentum flux or stress. While the presence of convection will be the key contrasting factor in my analysis, the variation of surface fluxes during different phases of the Madden-Julian oscillation (MJO) will also be noted. Using the time series of individual level legs (LL) to directly examine surface fluxes during periods with and without convection, I endeavor to better understand the coupled air-sea processes that

affect not only Indian Ocean surface fluxes but surface fluxes in general. Following this analysis of surface fluxes under convective and non-convective conditions, the in-situ data is compared with the outputs calculated from the Coupled Ocean Atmosphere Response Experiment (COARE) bulk surface flux parameterization algorithm. COARE is the state-of-the-art surface flux parameterization used in most mesoscale forecast models. This study provides an analysis of the applicability of COARE outputs to this region by comparing the output flux estimates from the COARE algorithm to fluxes calculated from in-situ data. Through comparison instances where the COARE algorithm provides a realistic parameterization of air-sea boundary fluxes for both convective and non-convective conditions as well as the Indian Ocean are provided.

II. BACKGROUND

A. TURBULENT FLUXES

Turbulent flux refers to the directional rate of transfer of a quantity across a unit area normal to the direction of transfer. For a quantity (ζ), the kinematic flux across the horizontal plane can be written as:

$$F = w\zeta \quad (1)$$

where w is the vertical velocity. Using Reynolds decomposition, we can write $w = \overline{w} + w'$, $\zeta = \overline{\zeta} + \zeta'$. Taking the Reynolds average on both sides of Equation (1), we get:

$$F = \overline{w\zeta} + \overline{w'\zeta'} \quad (2)$$

The first term of Equation (2) is referred to as advective flux and the second term as turbulent or eddy flux. The advective flux represents the transport of the mean quantity by mean vertical velocity. This term is generally small and negligible due to the small magnitude of the mean vertical velocity. The eddy flux represents the transport of the perturbations by the eddy vertical velocity relative to the mean vertical velocity. It is calculated by the mean product of the velocity and the transported quantity perturbations, a method usually referred to as eddy correlation method.

Stress is the force that produces deformation in a body. Shearing stress occurs when force is applied perpendicular to the normal face of a defined unit area. Reynolds stress results from the turbulent transport of momentum and is equivalent to the turbulent momentum flux due to turbulence resulting in deformation of a fluid parcel.

Using Reynolds decomposition and eddy-correlation method the fluxes at flight level can be calculated as in Kalogiros and Wang (2011) with momentum flux or stress as $\tau = \rho(\overline{u'w'^2} + \overline{v'w'^2})^{1/2}$, SHF as $H_s = \rho C_p \overline{w'\theta'}$, and LHF as

$H_l = \rho L_v \overline{w'q'}$ where ρ is the dry air density, C_p is the specific heat capacity of air at constant pressure, L_v is the latent heat of vaporization, u , v , and w are the horizontal and vertical wind components, q is the water vapor mixing ratio, and θ is potential temperature.

An alternative method for the estimation of surface fluxes is through the use of turbulence co-spectra. SHF is estimated by integrating the co-spectra of vertical velocity and potential temperature over the desired length-scale range to obtain the kinematic fluxes from contributions of eddy sizes within the range of length-scale integration. This practice is equivalent to those fluxes obtained from eddy-correlation method with a filtering window covering the same range of length scales as in the co-spectra integration. Kinematic LHF and stress can be similarly calculated using the co-spectra of vertical velocity and water vapor or horizontal velocity components, respectively.

A third method of flux calculation, often referred to as inertial dissipation method, is used in cases where platform motion cannot be separated from the dataset (Edson et al. 1991). This method utilizes the turbulence power spectra in the inertial subrange that allows the calculation of the turbulent dissipation rate. Turbulent momentum fluxes are then derived through parameterized relationship with the dissipation rate. Edson et al. (1991) provides the details of this method. It is not often used today due to significant improvements and miniaturization of inertial measurement units used to characterize ship or buoy motions.

B. PARAMETERIZATION FOR FORECAST MODELING

Surface flux processes must be parameterized because of their sub-grid spatial and small temporal scales. The formulation of such a parameterization in numerical weather prediction has been an area of extended research (e.g., Fairall et al. 1996b). The parameterizations themselves are developed through field experimentation with the guidance of basic surface layer theories. During these field experiments in-situ flux and bulk meteorological variable data collection occurs for a region of interest. Following the field experiment the data

is analyzed to develop linkages between the mean variables and surface fluxes. From this study, bulk formulas and transfer coefficients are developed that form the foundation for the air-sea flux parameterization (Fairall et al. 1996b). Follow-on field work seeks to fine tune the parameterization in different regions of the globe. This fine-tuning compares the bulk parameterization with regionally observed fluxes to establish the validity of the parameterization in comparison with the observed surface fluxes.

The COARE bulk surface flux parameterization algorithm is the focus for comparison in the following analysis. COARE was initially developed as part of the Tropical Ocean-Global Atmosphere (TOGA) program (Fairall et al. 1996b). The foundation of the COARE bulk algorithm is Monin-Obukhov similarity theory (MOST). Surface fluxes are determined through the bulk aerodynamic formulation. The bulk aerodynamic formulation is applied for a quantity (ϕ) as $F_\phi = \rho C_\phi U (\overline{\phi_{sfc}} - \overline{\phi})$ where F_ϕ is the surface flux of the quantity, U is the mean wind speed, and C_ϕ is the bulk aerodynamic transfer coefficient based on MOST (Vickers and Esbensen 1998). The inputs to the COARE bulk surface flux parameterization algorithm utilized in this analysis are flight level measurements of atmospheric pressure, temperature, relative humidity, wind speed, measurement height and latitude, and sea surface temperature (SST).

C. UNCERTAINTIES IN SURFACE FLUXES AND THEIR PARAMETERIZATION

Many factors contribute to uncertainties in the parameterization of surface fluxes. In addition to measurement and representation errors in the atmospheric variables directly involved in the bulk scheme, additional uncertainties are introduced due to the factors affecting the measurement of SST, gusts in low wind conditions, precipitation, and waves and swells. These uncertainties ultimately create discrepancies between the observed and parameterized surface fluxes affecting forecast accuracy.

Measurement of SST can be made by an infrared radiometer for skin temperature and/or a thermistor for bulk water temperature located below the immediate sea surface. Both methods require unique correction due to the nature of the measurements not capturing the true skin temperature. Infrared radiometers must be corrected for reflected atmospheric radiance as well as calibrated to near perfect accuracy and precision (Fairall et al. 1996a). Radiance correction involves the removal of all reflected atmospheric radiance and atmospheric path radiance within its field-of-view to find only the radiance transmitted from the sea surface to the sensor. When using a bulk temperature sensor the true SST may be cooler or warmer than the measured bulk temperature because bulk temperature sensors measure at a designed depth. Solar heating of the upper ocean may result in a top layer of a few meters that is warmer than the layer below, which is normally referred to as a “warm layer.” Meanwhile, a “cool skin” occurs due to cooling from the net loss of longwave radiation. Such a radiation deficit results in a skin temperature that is cooler than the bulk of the water below. The processes that cause warm layer and cool skin can occur simultaneously and are corrected for within the COARE bulk surface flux parameterization algorithm (Fairall et al. 2003).

Parameterization of surface fluxes may encounter difficulties in low wind conditions. This issue occurs due to the fact that the COARE bulk surface flux parameterization algorithm is directly related to the mean wind speed. The input mean wind speed utilized in the COARE bulk surface flux parameterization algorithm is the magnitude of the mean wind vector, $U = (\overline{u}^2 + \overline{v}^2)^{1/2}$, where component velocities are averaged separately before forming the parameterization’s velocity scale input. In calm and low wind conditions, gustiness in the wind perturbations still generates some surface exchanges of momentum and mass (Godfrey and Beljaars 1991; Vickers and Esbensen 1998). These gust-induced fluxes cannot be reflected in the original formulation of the bulk flux schemes due to the direct use of the mean wind speed. A gust velocity

is added to the velocity scale input to the bulk algorithm to mitigate this situation (Fairall et al. 1996b) following the work of Godfrey and Beljaars (1991).

Waves and swell generated by distant storms modify boundary layer turbulent fluxes and represent additional uncertainty in the original formulation of the surface flux parameterization. A passing swell imparts force on the environment causing momentum transfer to the atmosphere from the ocean as opposed to the original concept of wind forced ocean dynamics. This effect is most prominent in low wind conditions (Sullivan et al. 2008). Important factors in estimating stress during periods of swell are swell age, amplitude, and orientation to the mean wind. Measured drag coefficients used in the bulk aerodynamic formulation are influenced by strong swell where drag increases are significant when the wind opposes swell (Sullivan et al. 2008). While COARE does account for local wind conditions in surface roughness, it does not account for swell waves from distant source regions. The effect of swell is significant to surface stress and most problematic to the COARE bulk surface flux parameterization in low wind conditions (Fairall et al. 2003). Additionally, the wind wave effects on surface flux are parameterized through the Charnock relationship (Charnock 1955). Efforts have been made in the past to directly relate this effect to wave age or wave steepness, which is termed as the sea-state dependent surface flux parameterization (Hare et al. 1997; Kudryatsev and Makin 2004).

There is evidence that surface fluxes are significantly modified by convective processes due to their associated downdrafts and precipitation. Jabouille et al. (1996) indicated that downdrafts are specifically responsible for increases in surface fluxes by bringing cold and dry air in contact with the sea surface. Heat fluxes are enhanced due to the pairing of cold, dry air above the warm, moist sea surface. Additionally, downdrafts induce increased wind speeds resulting in increases in stress. Beyond the effects of downdrafts, precipitation associated with convection has been noted to cause an increase of two times in LHF and three times in SHF (Jabouille et al. 1996). Furthermore, rainfall effects stress due to momentum imparted to the ocean surface (Fairall et al. 1996b).

These processes will be discussed at length in the next section as the focus of this research is the effect of convective precipitation on surface fluxes.

D. CONVECTIVE COLD POOLS AND SURFACE FLUXES

Deep and shallow cumulus precipitation is most common over the tropical ocean. One of the long-term research topics related to precipitation is its effects on the subcloud layer and surface fluxes. Early studies have long recognized that the well-mixed subcloud layer that prevails in undisturbed conditions is modified by precipitating disturbances in a more stable structure (e.g., Echternacht and Garstang 1976) where moist downdrafts play an important role in the subcloud layer modification process. Two processes exist in the case of precipitation that increase the coupling between the cloud and subcloud layers and modify the subcloud mixed layer structure. Evaporation of precipitation hydrometers in the unsaturated subcloud layer is a heat sink and a source of water vapor. Such cooling effects bring the second controlling process: convective-scale downdrafts that bring down potentially warm and dry air into the subcloud layer. These two processes compete with each other and in most cases result in the subcloud layer being cooler and drier after the precipitation and downdrafts (Betts 1976). Consequently, the presence of a cold pool is often referred to behind the convective precipitation region.

Jorgensen et al. (1997) examined the development of cold pools under convection using aircraft measurements from the 1992 TOGA COARE field campaign based in the Solomon Islands. Airborne Doppler and in-situ measurements were used to depict the structure of mesoscale convective systems (MCS) as well as their associated cold pools. Jorgensen et al. (1997) identified cold pools rising to an altitude of 500 m below convective lines by locating the coldest air behind zones of high radar reflectivity. Important to this analysis was the finding that the boundary layer rapidly recovers following squall line passage through strong fluxes of latent and sensible heat from the warm ocean surface below (Jorgensen et al. 1997). The cold pool immediately below

the squall line shows the strongest cooling and drying as depicted in the example shown in Figure 1 when the aircraft penetrated at 150 m across the gust front of a squall line. Figure 1 indicates that the aircraft clearly penetrated the heavy rain region of the convective line roughly between the end points of the arrow on the θ_e plot. Increased westerly winds, colder temperatures, and lower mixing ratios can be identified to correspond to penetration of the outflow air. The higher values of q and the northerly winds at the end of the leg appear to be those of the environment.

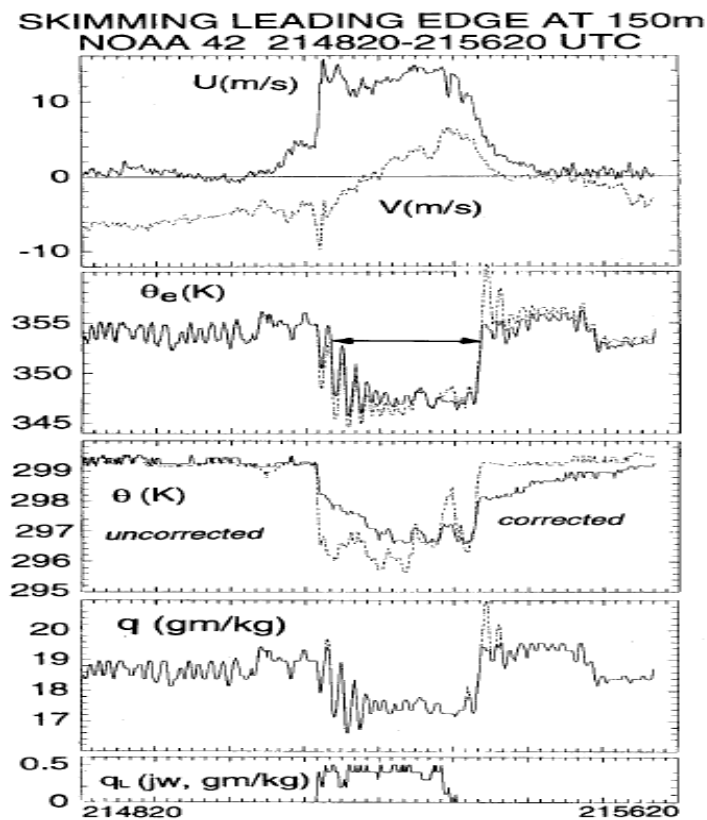


Figure 1. Time series of in-situ data collected during the penetration of a gust front (from Jorgensen et al. 1997).

Figure 2 shows a comparison of the vertical profiles at different locations relative to the convective cloud. The solid line shows the undisturbed boundary layer profiles, dash lines show soundings in the precipitation disturbed boundary

layer, and the dash-dot line reveals the vertical profile that recovered gradually. The potential temperature profiles show distinct differences in the mixed layer depth, about 500 m in the undisturbed boundary layer, lowered to ~200 m behind the gust front with temperature about 2.5 K cooler. At 120 km behind the gust front, the boundary layer is still recovering from the disturbance with both θ and q lying between the undisturbed and highly disturbed environment. It is also seen that the tropical mixed layer is not at all well-mixed in water vapor in its undisturbed state, but was much better mixed in the disturbed and recovered stage. This seems to indicate the enhanced mixing by the enhanced surface fluxes or by convective scale downdrafts.

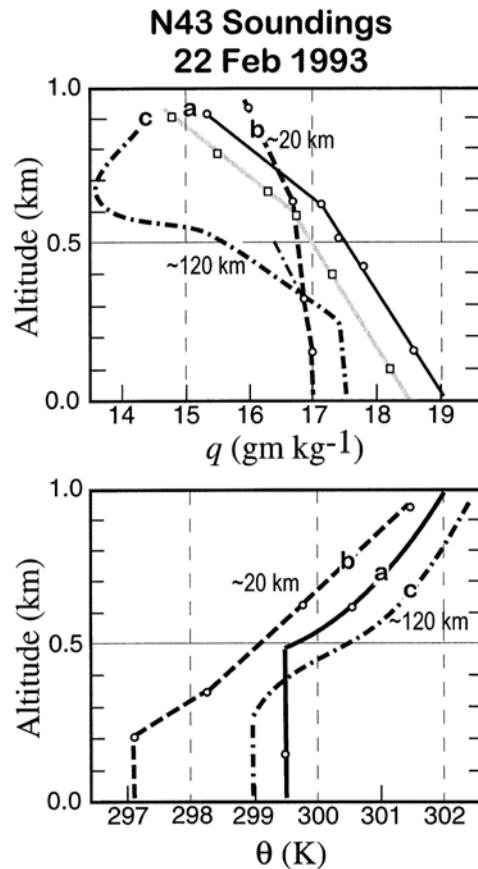


Figure 2. Comparison of specific humidity and potential temperature in undisturbed (solid), highly disturbed (dash), and recovering (dash-dot) boundary layers at the indicated distances to the leading edge of a convective gust front (from Jorgensen et al. 1997).

Following Jorgensen et al. (1997), Tompkins (2001) made numerical simulations to study the organization of tropical convection and the role of cold pools in initiating new convection. He found out that under deep convection, cold pools develop mainly due to injection of cold, dry air and enhanced wind speeds into the boundary layer by downdrafts. Coming into contact with the ocean surface the cold, dry downdraft air spreads horizontally outward as in Figure 3. When the downdraft is no longer sustainable the cold pool recovers from the center outward due to entrainment of air from above the boundary layer (Tompkins 2001). Tompkins attributed continued convection to cold pools lifting the atmospheric boundary layer allowing free convection to occur due to their tendency to spread outward. In these regions, surface fluxes increase due to the introduction of dry, cold air and enhanced wind speeds from the downdraft (Tompkins 2001).

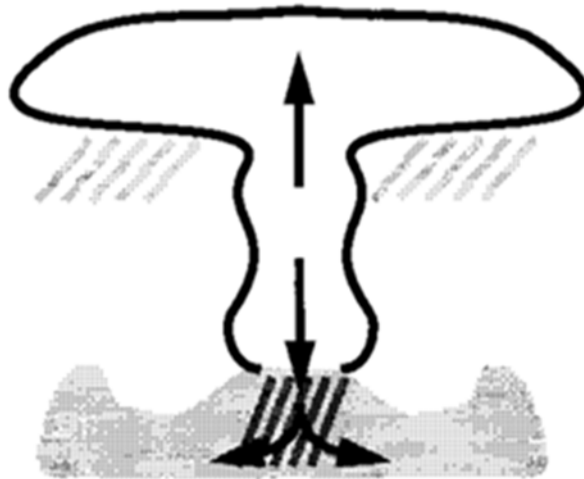


Figure 3. Schematic of cold pool development and spreading under deep convection (from Tompkins 2001).

Corfidi (2003) found similar results that confirm the role of latent cooling of precipitation in generating the cold pool while the increased wind induced by the downdraft expands the cold pool. Cold pools are not symmetric bodies due to the

mean wind direction. The mean wind reorganizes the cold pool by elongating the cold pool along the mean wind (Corfidi 2003). Linked to the modeling of Tompkins, Corfidi (2003) observed as the downwind edge of the cold pool extends outward it can undercut the local air mass thereby forcing it to rise upward triggering new convection (Corfidi 2003). This process is illustrated in Figure 3.

Zuidema et al. (2012) analyzed the data from the Rain in Cumulus over the Ocean (RICO) experiment with the focus on shallow precipitating cumulus by looking into the boundary layer recovery from the cold pool. They hypothesized, based on previous study, that the boundary layer recovery process is sensitive to the organization of convection. Zuidema et al. (2012) defined cold pools beyond a region of cold air surrounded by warmer air, further linking cold pool formation and recovery to the onset of surface rain and the recovery of temperature following the rain event. They noted from the RICO data that rain events typically accompanied increased wind speeds (Zuidema et al. 2012). Subsequently, increased surface winds from downdrafts resulted in drier, cooler surface air and subsequent increases in SHF and LHF as previously observed. Yet as cold pools recovered, SHF returned to pre-rain magnitudes while LHF remained constant along with wind speed (Zuidema et al. 2012).

E. MADDEN-JULIAN OSCILLATION AND TROPICAL CONVECTION

The MJO is a tropical disturbance that propagates eastward around the global tropics with a cycle on the order of 30–60 days. It has broad impacts on the patterns of tropical and extratropical precipitation, atmospheric circulation, and surface temperature around the global tropics and subtropics (e.g., Hendon and Glick 1997; Thompson and Roundy 2013). A MJO event covers a broad area with regions of strong, well-organized tropical convection and weak convection while traveling eastward. From an Eulerian point of view, at a given location, the MJO event will pass the location with different phases of the convection, the active phase or the inactive phase (Zhang 2005). A geographic point along the

line of eastward propagation will experience weak convection in the leading inactive area, followed by strong convection in the central active area, trailed by weak convection of the western inactive area (Zhang 2005).

Geographic coverage and eastward propagation are important characteristics of the MJO. The central active phase covers a much smaller area than the bounding inactive phase areas (Zhang 2005). Consequently, at a given time a smaller surface area experiences strong active phase convection compared to weak inactive phase convection. Eastward propagation occurs due to the adjacent development of new convective systems over warm surface waters to the east of the older convective systems (Zhang 2005). As the excess of available potential energy for upward vertical motion is dissipated from the sea surface the older convective systems to the west collapse and join the area in inactive phase. In this continuing motion the MJO propagates across the Indian Ocean and western Pacific Ocean as in Figure 4 (Zhang 2005).

Due to the transient nature of MJO events and the presence of convective precipitation in both the active and inactive phase of the MJO, the precipitation enhanced surface fluxes associated with convective precipitation may be rather sporadic and transient. Conversely, due to the extended coverage of the cold pool, the overall coverage of the enhanced flux area may be significant enough to make sizable contributions to the tropical air-sea exchange. This thesis research aims to quantify the surface fluxes in both convective and non-convective conditions in all phases of the MJO and attempt to understand the difference in the nature of turbulent transport in different phases of the MJO. The ultimate goal is to assess the capability of a current bulk surface parameterization in representing surface exchanges in all conditions.

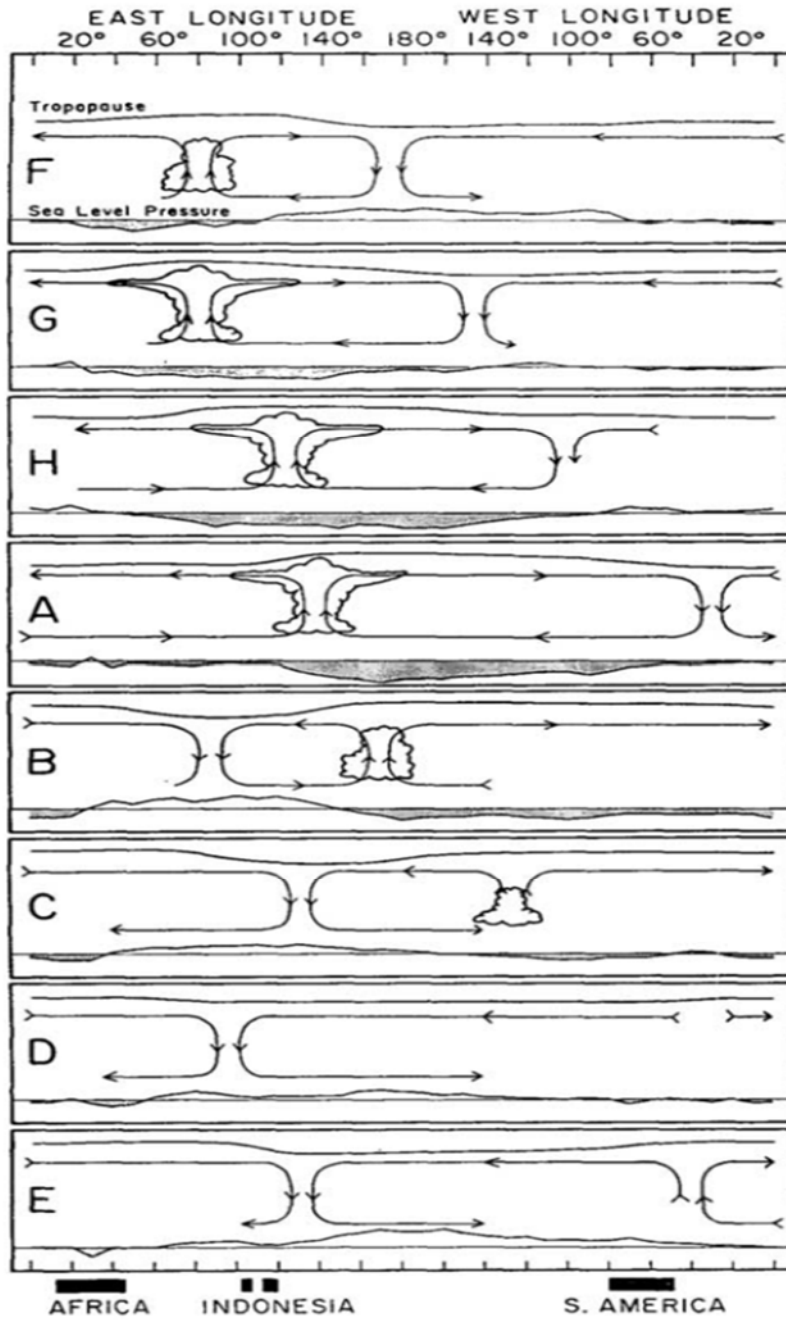


Figure 4. Schematics of the MJO convective region and its eastward development (from Zhang 2005).

III. AIRCRAFT MEASUREMENTS IN LASP/DYNAMO

A. OVERVIEW

The LASP/DYNAMO aircraft campaign made 12 research flights with the National Oceanic and Atmospheric Administration (NOAA) WP-3D Orion (N43, hereafter P-3, Figure 5) based from Diego Garcia in the British Indian Ocean Territory. The P-3 is a four-engine turboprop capable of operating at 170 to 250 knots indicated airspeed. At low altitudes the P-3 is capable of operating for up to 9.5 hours to a range of 2,500 nautical miles and at high altitudes the P-3 is capable of operating for up to 11.5 hours to a range of 3,800 nautical miles (NOAA Air Operations Center 2014).



Figure 5. NOAA Lockheed WP-3D Orion (from NOAA Air Operations Center 2014).

P-3 measurements occurred between November 11, 2011, and December 13, 2011, with an initial test flight, 10 science flights, and a final instrument calibration and comparison flight. Each of the DYNAMO science flights had one of two research foci: convection or boundary layer focused sampling. Table 1 lists all P-3 flight dates and their research foci. Their measurement date relative to the different phases of the November 2011 MJO event is also given in the

table (Wang et al. 2013). The data utilized in this study includes measurements from all flights.

Table 1. LASP/DYNAMO flight summary (after Wang et al. 2013).

Flight	Date	Science Objective	MJO Phase
RF01	11-Nov-11	convection	pre-active
RF02	13-Nov-11	boundary layer	pre-active
RF03	16-Nov-11	convection	pre-active
RF04	19-Nov-11	boundary layer	pre-active
RF05	22-Nov-11	convection	active
RF06	24-Nov-11	convection	active
RF07	26-Nov-11	boundary layer	active
RF08	28-Nov-11	boundary layer	active
RF09	30-Nov-11	convection	active
RF10	4-Dec-11	boundary layer	post-active
RF11	8-Dec-11	convection	post-active
RF12	13-Dec-11	boundary layer	post-active

The DYNAMO operations area was defined by the islands of Diego Garcia and Gan as well as the research vessel (R/V) *Roger Revelle* and R/V *Mirai* as shown in Figure 6. Some research flights were made outside the established DYNAMO operations area to investigate specific meteorological processes and phenomena of interest.

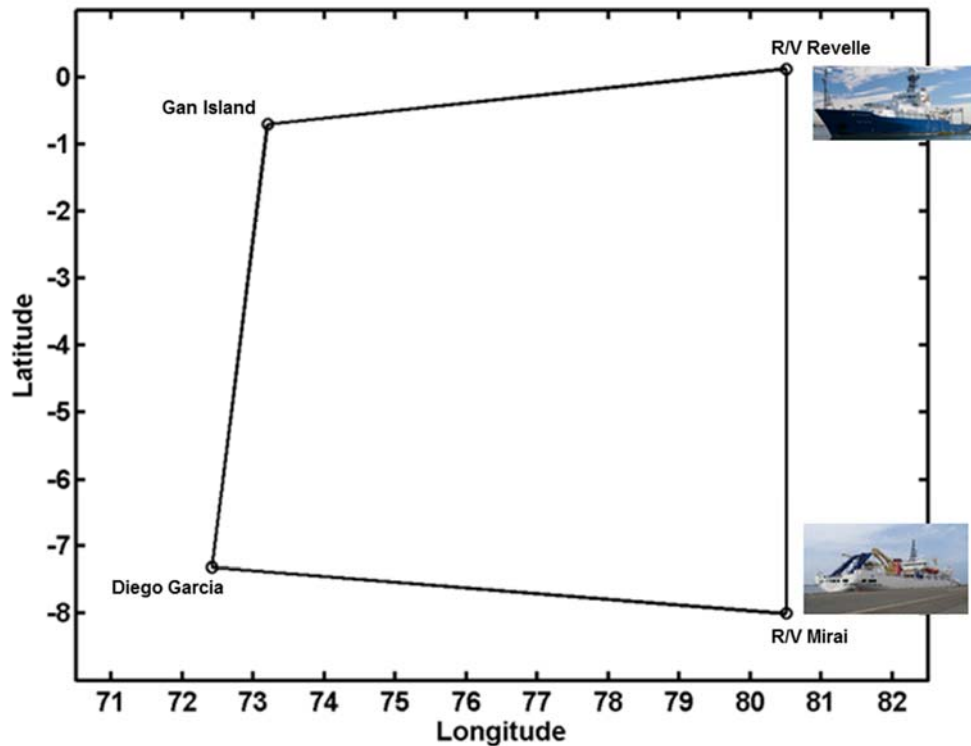


Figure 6. DYNAMO operations area.

B. DATA COLLECTION MODULES AND VARIABLES

Each P-3 flight was executed with different modules focusing on boundary layer, convection, and dropsonde deployment, respectively. Boundary layer modules consisted of flight-level vertical stack (FVS), flight-level cross-section, or flight-level flux mapping (FFM) modules. Convection modules consisted of dropsonde cloud survey or radar convective element maneuver. Dropsonde modules include a dropsonde area survey module and a dropsonde convective element module. This thesis work will focus only on data from FVS and FFM modules as well as individual LL sampled below nominally 75 m.

The FVS module is designed to sample vertical variation in meteorological variables and air-sea fluxes within the boundary layer. It contains a stack of LL on the same bearing at various altitudes within the atmospheric boundary layer. Each LL at a constant level is typically 10 minutes in duration. At the end of the

LL, the aircraft conducts a reversal of direction and adjusts to another altitude. Usually, there are four altitudes sampled in a single FVS module. This may vary due to the available flight time and the depth of the boundary layer. Figure 7 illustrates the legs of the FVS module. Note that the highest leg is designed to be within the cumulus cloud. It is thus technically above the tropical boundary layer, which is normally defined at the cumulus cloud base (LeMone 1973).

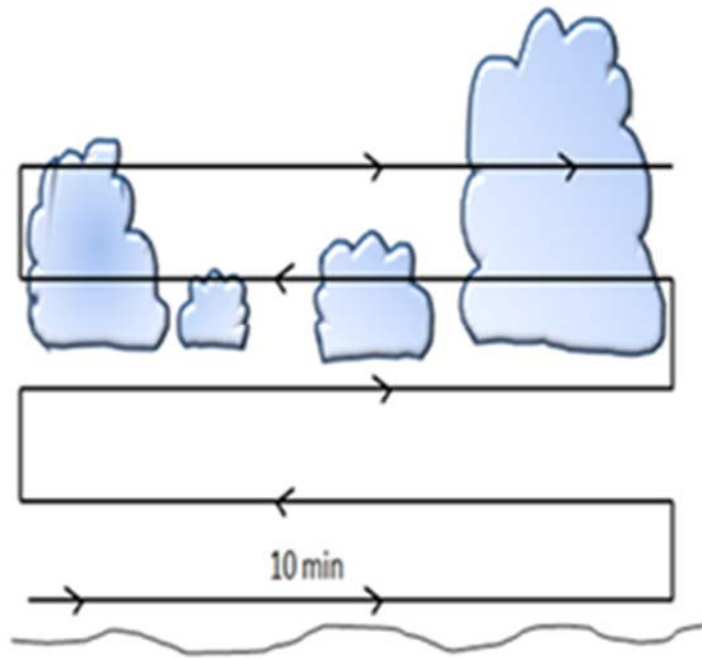


Figure 7. FVS maneuver used in the LASP/DYNAMO experiment (from Wang et al. 2013).

The FFM module samples the boundary layer at a constant altitude with some spatial coverage to sample a geographic region. The FFM makes a lawn-mowing pattern with long legs about 10 minutes in duration and short legs of about two minutes in duration. Figure 8 shows a schematic of the FFM module. This module is designed to sample horizontal variation in meteorological variables and air-sea fluxes within the boundary layer at the lowest possible level allowed by flight safety.

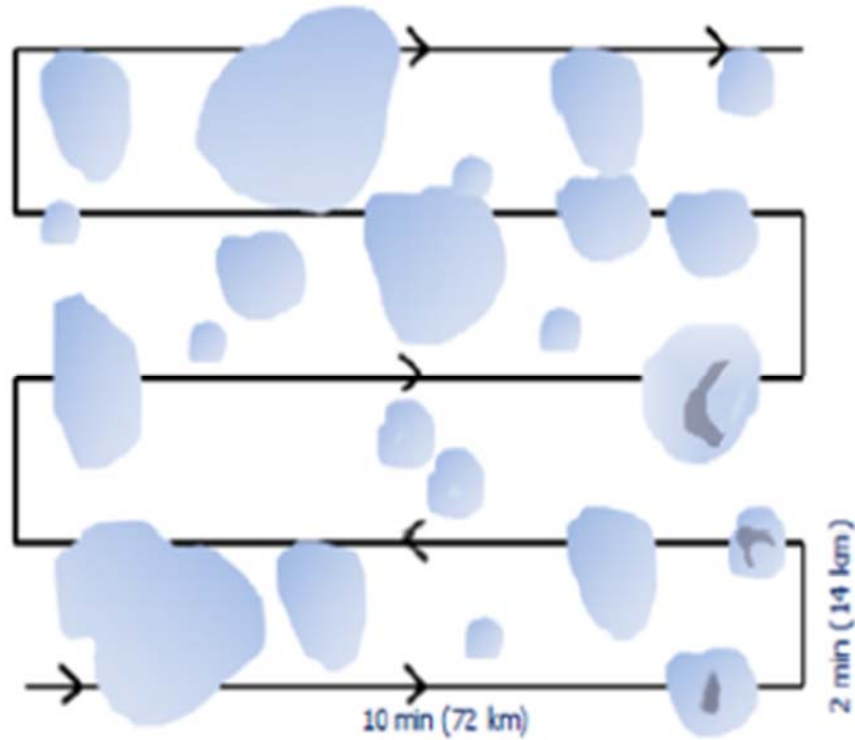


Figure 8. FFM maneuver used in the LASP/DYNAMO experiment (from Wang et al. 2013).

The data utilized in this analysis was collected at sampling rates of 1 Hz or 25 Hz per Table 2. The 25 Hz data was used to calculate turbulent fluxes and to perform spectral analyses. At a nominal flight speed of 120 m s^{-1} for the P-3, the spatial resolution of P-3 high-rate measurement is about 4.8 m.

Table 2. LASP/DYNAMO measured or derived variables used in this study and their sampling rates.

Parameter	Sampling Rate	Units
Absolute humidity	25Hz	g m^{-3}
Altitude	1Hz, 25Hz	m
Ambient temperature	1Hz, 25Hz	$^{\circ}\text{C}$
Dew point temperature	1Hz, 25Hz	$^{\circ}\text{C}$
Fuselage true airspeed	1Hz, 25Hz	m s^{-1}
Heading	1Hz, 25Hz	degrees
Latitude	1Hz, 25Hz	$^{\circ}\text{N}$
Longitude	1Hz, 25Hz	$^{\circ}\text{E}$
Potential temperature	1Hz, 25Hz	K
Pressure	1Hz, 25Hz	hPa
Relative humidity	1Hz	%
Sea surface temperature	1Hz, 25Hz	$^{\circ}\text{C}$
"Sky" temperature	1Hz, 25Hz	$^{\circ}\text{C}$
Specific humidity	1Hz	g kg^{-1}
Time	1Hz	seconds from Global Positioning System epoch
Time	25Hz	year, month, day, hour, minute, second
Wind component (East direction)	25Hz	m s^{-1}
Wind component (North direction)	25Hz	m s^{-1}
Wind component (Vertical direction)	25Hz	m s^{-1}
Wind direction	1Hz, 25Hz	degrees
Wind speed	1Hz, 25Hz	m s^{-1}

C. SUMMARY OF FLIGHT CONDITIONS AND LOW LEVEL LEGS FOR EACH FLIGHT

RF01 occurred during clear skies with scattered cumulus and patches of high cirrus clouds along the eastern side of the DYNAMO operations area. The flight was conducted west of the DYNAMO operations area into a disorganized convective line oriented southwest to northeast. The P-3 completed nine LL and further analyses were made on the three LL below 75 m.

RF02 occurred during a period of clear, fair weather with some cumulus clouds. The P-3 transited along the southern and eastern boundaries of the DYNAMO operations area followed by air-sea sampling modules in the area's northeastern corner before returning to Diego Garcia per Figure 9. The P-3 air-sea sampling area was west of the R/V *Revelle*. The proximity of the two

platforms allowed for ship-aircraft inter-comparison to be conducted. The P-3 completed 15 LL and further analysis occurred on the 12 LL below 75 m and the five LL as part of a single FVS module.

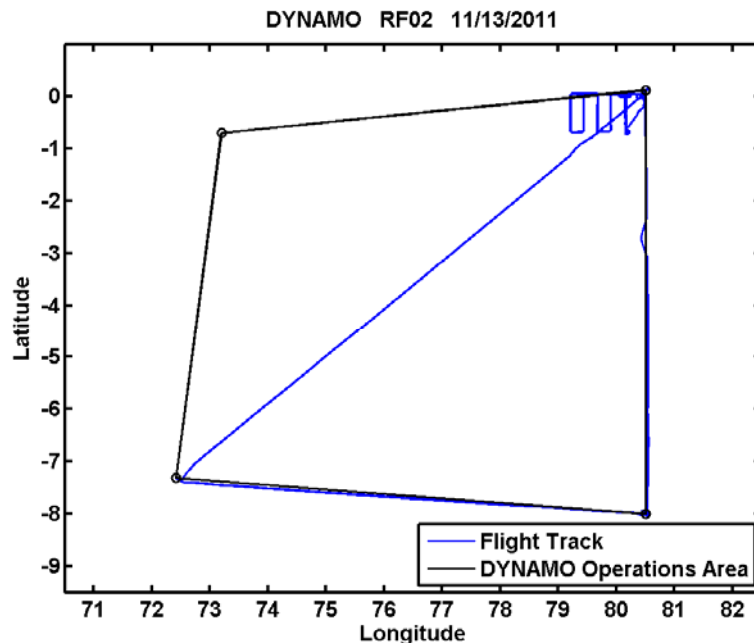


Figure 9. RF02 P-3 flight track (blue) on November 13, 2011.

RF03 occurred while convective cells broadly covered Diego Garcia and the southern half of the DYNAMO operations area. The P-3 operated in a convective region near Diego Garcia transiting south until breaking out of the convective region, turning north to the northwest corner of the DYNAMO operations area, and then returning to Diego Garcia. The P-3 completed 17 LL legs and this thesis work involves further analysis on the seven LL legs below 75 m.

RF04 occurred while a large area of organized convection to the west and a smaller area of organized convection along the eastern boundary bounded the DYNAMO operations area. The P-3 conducted multiple FVS modules while transiting northeast to the center of the DYNAMO operations area in a cumulus-topped environment before returning to Diego Garcia. Thirty-five LL were

completed where further analysis occurred on the 11 LL below 75 m and the five FVS profiles consisting of five LL each.

RF05 was made in a deep convection environment to the northeast corner of the DYNAMO operations area. This flight occurred at the onset of the November 2011 MJO event. The P-3 conducted convective sampling through the area's center into the northeast corner of the DYNAMO operations area. Eighteen LL were completed and further analysis occurred on the seven LL below 75 m.

RF06 occurred while extensive cloudiness covered the Indian Ocean from the DYNAMO operations area northward, marking the full-blown MJO active event. Westerly winds fed vigorous convection in the northeast corner of the DYNAMO operations area where the P-3 sampled. The P-3 completed nine LL and further analysis occurred on the two LL below 75 m.

RF07 occurred while broad upper level cirrus aligned southwest to northeast across the DYNAMO operations area. The P-3 transited to and from the northeast corner of the DYNAMO operations area where air-sea sampling maneuvers were conducted in the vicinity of overcast conditions and a few small showers. Again, this flight was made nearly collocated with the R/V *Revelle*. Twenty-five LL were completed and further analysis occurred on the 17 LL below 75 m and five LL forming a single FVS profile.

RF08 occurred while cumulus covered Diego Garcia with cloudiness and convection extending broadly across the DYNAMO operations box. The P-3 sampled east and southeast of Diego Garcia into two convective lines. Twenty-one LL were completed and further analysis occurred on the nine LL below 75 m and the four LL forming a single FVS profile.

RF09 occurred while cloud free skies existed throughout a majority of the DYNAMO operations area. Organized convection was identified south of Diego Garcia where the P-3 conducted convective maneuvers on convective

complexes and precipitating areas south of Diego Garcia. The P-3 completed 13 LL and further analysis occurred on the three LL below 75 m.

RF10 occurred while scattered cirrus extended along the southern boundary of the DYNAMO operations area with clustered convection near Diego Garcia. The P-3 conducted sampling in and around convection near Diego Garcia completing 25 LL. Further analysis occurred on the 12 LL below 75 m and the two FVS profiles of six LL each.

RF11 did not yield suitable boundary layer LL for further analysis due to the flight objective, which was observation of the three-dimensional structure of convective systems.

RF12 occurred while convective conditions existed northeast of the DYNAMO operations area and scattered convection extended west of Diego Garcia with some showers in the vicinity of Diego Garcia. The P-3 operated in the vicinity of Diego Garcia completing 11 LL. Further analysis occurred on the four LL below 75 m per Table 3.

Table 3. Summary of all low LL used in this thesis analysis.

Flight	Takeoff (UTC)	Landing (UTC)	Convection	LL below 75 m	FVS Modules
RF01	07:03	10:34	yes	3	0
RF02	03:12	12:34	no	12	1
RF03	04:06	13:02	yes	7	0
RF04	03:43	12:29	no	11	5
RF05	02:06	12:08	yes	7	0
RF06	01:28	11:17	yes	2	0
RF07	03:15	12:53	no	17	1
RF08	02:07	11:22	yes	9	1
RF09	01:36	11:33	yes	3	0
RF10	02:02	12:07	yes	12	2
RF11	04:27	12:11	no	0	0
RF12	03:09	07:37	no	4	0

THIS PAGE INTENTIONALLY LEFT BLANK

IV. DATA ANALYSIS METHODS AND RESULTS

A. DEFINING LEVEL LEGS

Aircraft measurement of turbulence cannot be effectively accomplished at large angles of aircraft pitch and roll. To eliminate the inaccuracies in turbulence retrieval due to pitch and roll, one can only use the portion of the data when the aircraft is flying along a straight path and at a constant level referred to as a level leg. A level leg is defined as a period when the aircraft is maintaining the required straight and level flight. Aircraft measurements from LL are studied extensively in this thesis research. My initial data analysis was to clearly define the usable data section when the measurements were intended to be at a constant level without significant heading change. This definition became the data section selection criteria for LL. Thus, selection of LL was based on an analysis of simultaneous aircraft altitude and heading. The beginning of a LL was established with the P-3 steadying on a predefined altitude and heading. The LL continued until the aircraft deviated from constant heading or altitude. Time series of altitude and heading were plotted and zoomed into a specific time period. The beginning and ending of the LL was then hand selected using MATLAB's "ginput" command.

Figure 10 shows an example of temporal variations of altitude and heading for RF08. The zoomed-in section of this plot was used to manually identify the start and end of each leg. Note with a moving platform such as an aircraft, the temporal variation shown in this figure reflects both spatial and temporal variations and is sometimes dominated by spatial variations. Figure 11 displays the identified LL plotted and color-coded with altitude. Each level leg is labeled in sequence with the number at the end of the flight track.

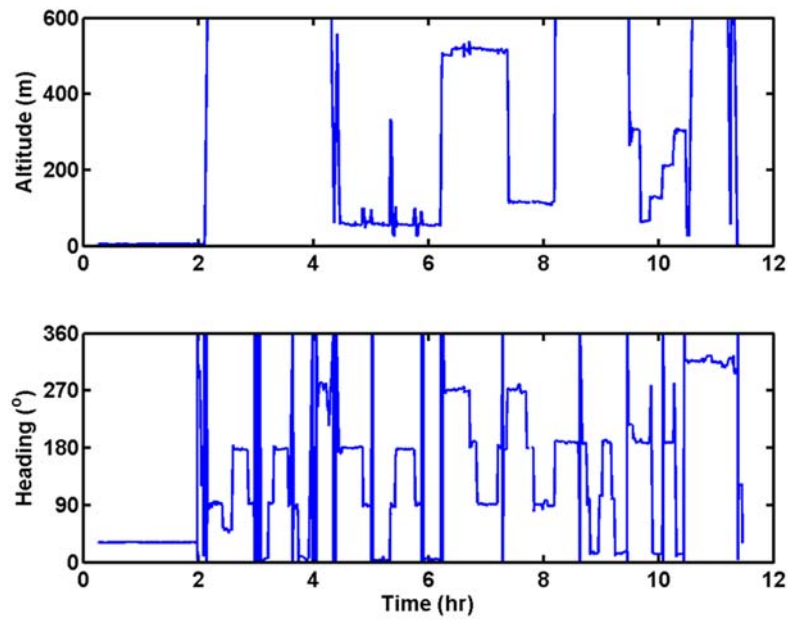


Figure 10. Aircraft altitude and heading for RF08. Time is in coordinated universal time (UTC).

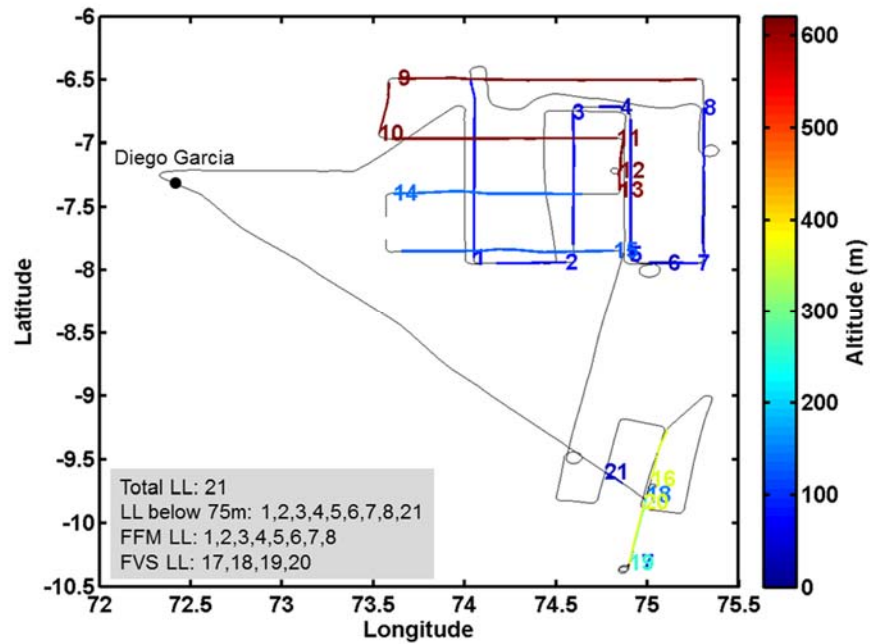


Figure 11. Aerial view of RF08 flight track (light gray) and all level legs. The altitude of measurement for each LL is indicated by the color bar.

B. SEA SURFACE TEMPERATURE CORRECTION

Accurate SST is crucial to quantifying air-sea fluxes using bulk parameterizations and understanding air-sea processes. Two types of SST corrections were attempted in this thesis work, one related to reflected radiance from the sky, one related to the emission of water vapor between the aircraft altitude and the surface.

Lind and Shaw (1989) showed that corrections were required for the radiometric SST to remove the effect of the skyward radiance reflected off the sea surface to the sensor. Reflected radiance was corrected for by Lind and Shaw (1989) with Equation (3):

$$SST = \left(\frac{1}{\varepsilon} T_{sfc}^4 - \frac{\alpha}{\varepsilon} T_{sky}^4 \right)^{1/4} \quad (3)$$

where $\varepsilon = 0.986$, $\alpha = 1 - \varepsilon$, T_{sfc} is the surface temperature measured by the downward looking radiometer, and T_{sky} is the sky temperature measured by the upward looking radiometer. This effect results in over-estimated SST. These two radiometric temperature variables were available from the P-3 measurements in LASP/DYNAMO.

The radiometric sea surface temperature measurements intend to obtain the SST through the measured irradiance from the ocean surface. However, the irradiance measurements inevitably include the emission of water vapor in the lowest levels. Consequently, the radiometric SST may vary depending on the altitude of measurements and the amount of water vapor below. The error introduced this way can be significant in the moist tropical environment and needs to be corrected. As temperature decreases with height in most tropical boundary layers, this water vapor effect on radiometric SST measurements results in under-estimates of the SST.

For LASP/DYNAMO, the correction for the SST can be obtained by a comparison of SST measurements from the P-3 against the top level water temperature from airborne expendable bathythermographs (AXBT) or airborne

expendable conductivity, temperature, and depth (AXCTD) probes. During the 12 flights of LASP/DYNAMO, a total of 428 AXBT/AXCTD probes were deployed. We identified all AXBT/AXCTD profiles concurrent and collocated with the low-level LL with radiometric SST measurements. The “SST” from these profiles is defined as the average water temperature of the top 1 m of the water temperature profile, which is referred to as the top water temperature to indicate its difference from the skin temperature of the surface. A comparison of these SST is given in Figure 12. Note that the data points used in this figure are from SST collected on LL below 100 m only.

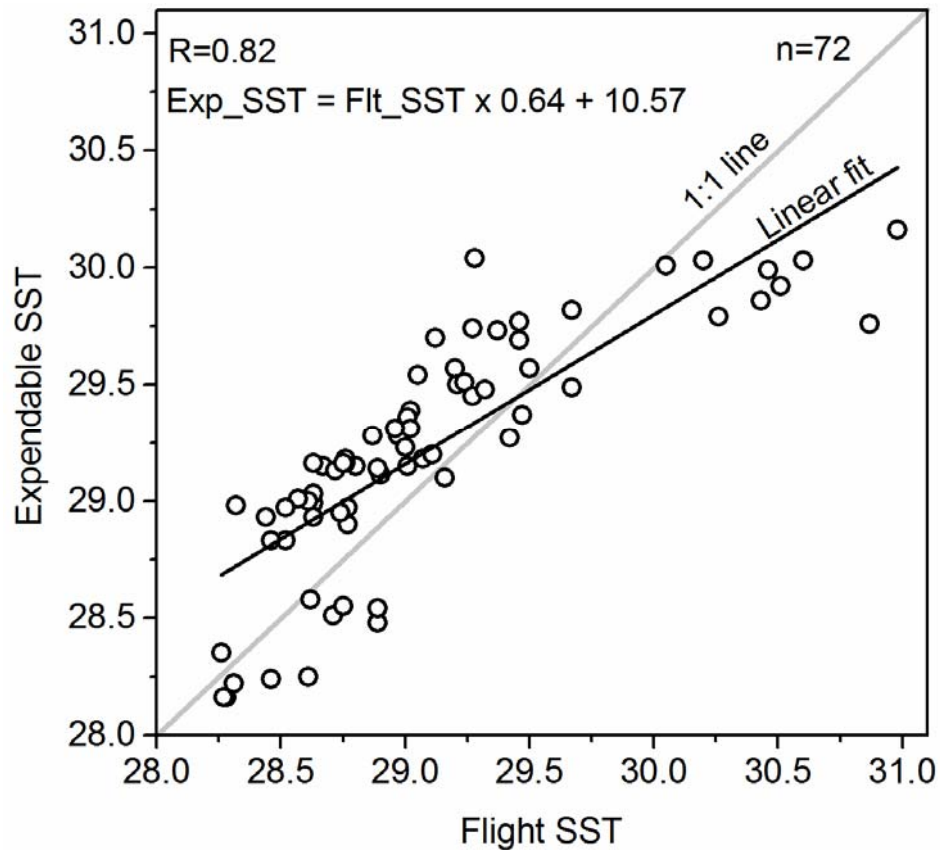


Figure 12. Comparison of collocated aircraft radiometric SST with AXBT/AXCTD top water temperature from LASP/DYNAMO (courtesy of Dr. Denny Alappattu).

Figure 12 shows that the difference between the radiometric SST and the top water SST is not constant. The reflected irradiance corrections dominate in warm water conditions, while the water vapor effects are most apparent in relative cool water. A linear fit between the two was obtained as the SST correction formulation for the LASP/DYNAMO cases and is given in Equation (4):

$$SST = 0.64T_{sfc} + 10.57 \quad (4)$$

where T_{sfc} is the surface temperature measured by the downward looking radiometer on the P-3. Equation (4) is used to make SST corrections to the radiometric measurements. It is worth mentioning that the top water temperature may be different from the true skin temperature due to the warm layer and cool skin effects (Fairall et al. 1996a). The corrected SST may still have some uncertainties that affects the COARE estimated fluxes.

C. SEPARATION OF CONVECTION AND NON-CONVECTION REGIONS

The objective of this thesis work is to examine the effects of convection on surface fluxes. For this reason, the data was separated into convective and non-convective cases. The selection of time periods for convective activity was taken from the work of Wang et al. (2013). Figure 13 shows an example of visible satellite image over the DYNAMO region overlaid with P-3 flight track on November 22, 2011 (RF05). The convective region in this example is identified by the area covered by the presence of extensive cloudiness (circled area). Convective regions from other flights are identified in similar manner based on satellite images at the time of the flight.

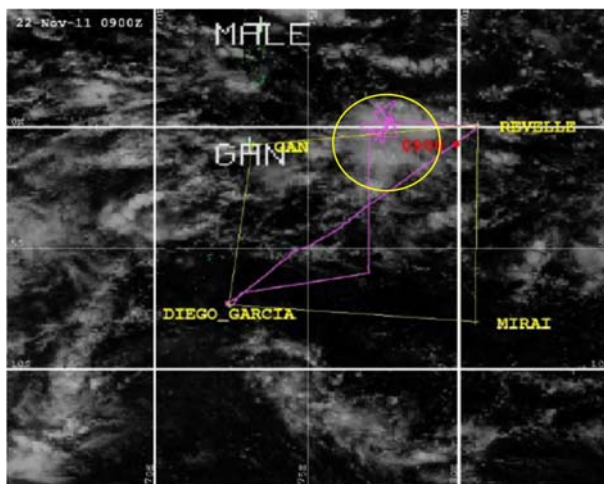


Figure 13. Visible satellite imagery on 0900 UTC, November 22, 2011 (RF05). The convective region is identified as the area covered by deep convective clouds (after Wang et al. 2013).

D. CALCULATING TURBULENT FLUXES

Following separation into convective and non-convective conditions the fluxes for each level leg were calculated using eddy correlation method and a 10 km averaging window. Only data collected on LL below nominally 75 m were utilized to ensure that the measurement level remained within the surface layer. Level leg averages of key input variables for the COARE surface flux parameterization were calculated using the same 10 km averaging window used to compute surface fluxes. This ensured the inputs to the COARE algorithm, such as altitude, latitude, temperature, pressure, relative humidity, sea surface temperature, and horizontal wind components, were coincident with the measured fluxes. Using LL mean inputs the COARE bulk surface flux parameterization produced estimates of parameterized surface fluxes. These fluxes were then compared to the eddy correlation method fluxes in the analysis to be shown in later subsections. Furthermore, the same data section for calculating fluxes was used to make spectral analyses that generated the power spectra and co-spectra of vertical velocity, potential temperature, and water vapor. This spectral analysis was done to identify the different spatial scales which contribute to surface flux under convective and non-convective conditions.

E. OVERALL COMPARISON OF TURBULENT FLUXES

Turbulent fluxes of momentum, sensible heat, and latent heat were computed from 85 level legs below 75 m from 12 LASP/DYNAMO research flights. Flux calculation used 10 km non-overlapping segments from each identified LL within the surface layer. This 10 km averaging window was adopted for comparison purposes between LL of different lengths. A level leg that is 30 km long will be represented by 3 flux values while a LL which is 10 km long will be represented by 1 flux value. The entire data set of eddy correlation method surface fluxes is displayed by flight in Figure 14 to provide an overview of the flux dataset. Convective and non-convective conditions are indicated by red points and blue points respectively. First glance of the fluxes indicate substantial variability of the flux within each research flight. LHF is in the range of a few up to 200 W m^{-2} , SHF ranges -10 and 25 W m^{-2} , and stress varies up to 0.18 N m^{-2} for all the flights. When comparing convective conditions (red) to non-convective conditions (blue) on Figure 14, the LHF does not appear to vary appreciably more for convective conditions compared to non-convective conditions. In contrast, the plot of SHF and stress clearly show an increased variability of flux under convective conditions.

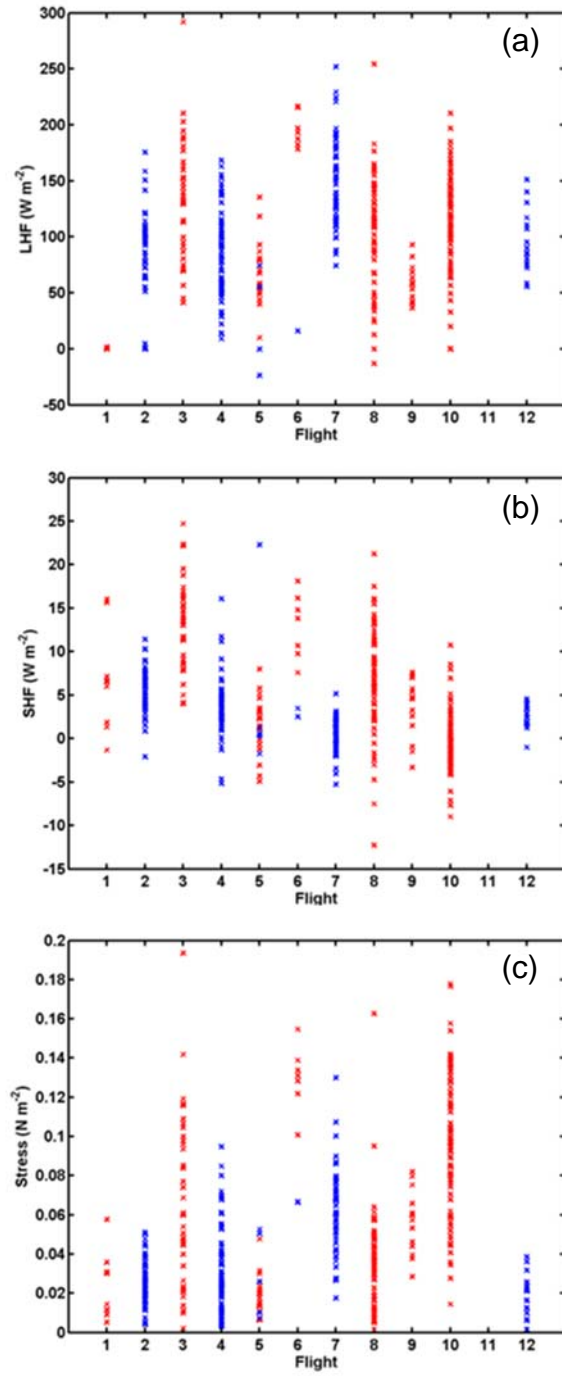


Figure 14. Low level turbulent fluxes from eddy correlation method for all flights for (a) LHF, (b) SHF, and (c) stress. Red points represent convective cases and blue points represent non-convective cases.

The results in Figure 14 are further represented in boxplots shown in Figures 15–17 to emphasize some of the statistics. It is clear in these figures that the median fluxes under convection (red) exceed those not under convection (blue). LHF (Figure 15) has the smallest increase and only appears to be slightly greater under convection, as shown in Figure 14. The extreme values of non-convective LHF for RF06 in Figure 15 are a result of only three data points and should be ignored. SHF (Figure 16) and stress (Figure 17) show greater proportional increases in flux for the convective cases. The vertical lines separate the phases of the MJO on Figures 15–17. Previous studies on MJO indicated increased turbulent fluxes in the MJO active phase (Young et al. 1995). This increase is not apparent in the LASP/DYNAMO observed fluxes, except for LHF (Figure 15).

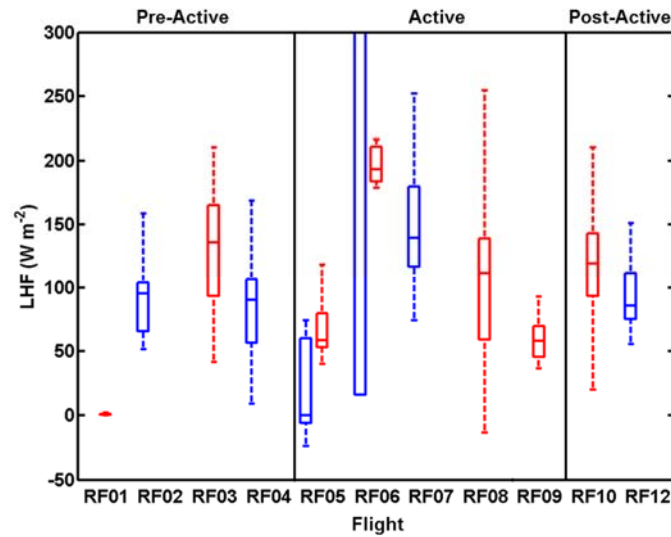


Figure 15. Boxplots of LHF calculated by eddy correlation method for each flight. Phases of Madden-Julian oscillation are separated by vertical lines. Convective cases are in red and non-convective cases are in blue.

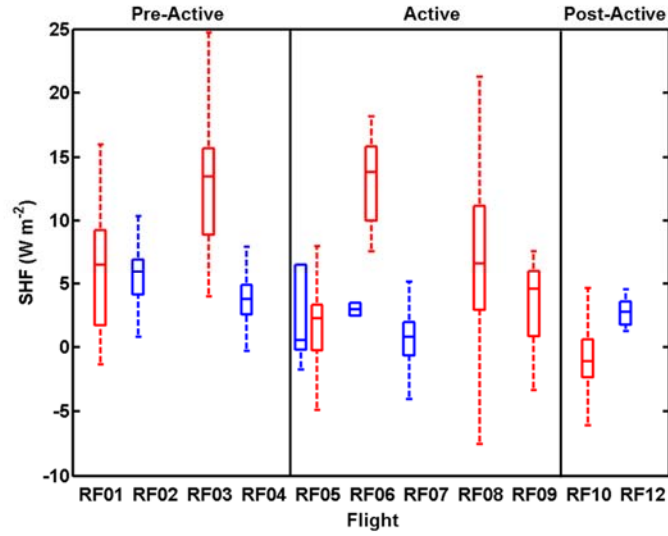


Figure 16. Same as in Figure 15, except for SHF.

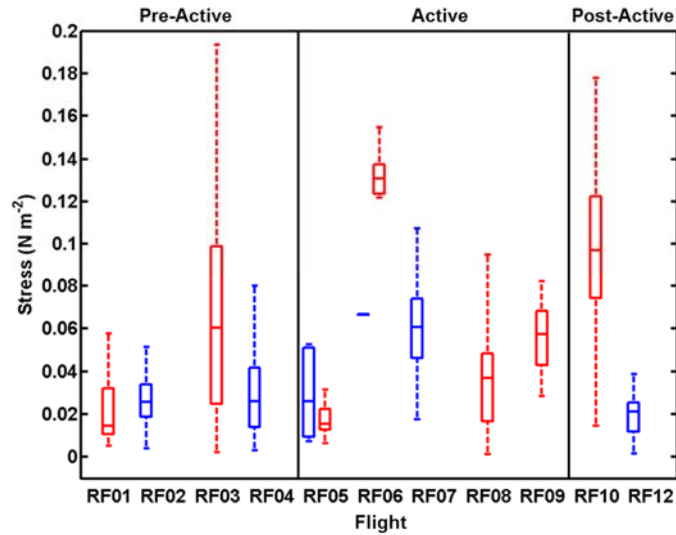


Figure 17. Same as in Figure 15, except for stress.

F. CHARACTERISTICS OF TURBULENT FLUXES

Comparisons of surface fluxes during periods of convective and non-convective activity are the focus of this section. Here, fluxes are grouped for all convective and non-convective cases separately and the variation of fluxes with sampling altitudes, air-sea temperature difference, and wind speed are

examined. Figure 18 shows the flux variation with height in the lowest 85 m. Note that the altitude used in this plot is from the high-rate data, which we believed to over-estimate the altitude by 10 m. Hence the actual altitude should be about 10 m lower. Figure 18a shows in the non-convective cases a clear trend of reduced LHF with altitude. This does not seem to be the case for the convective condition (Figure 18b). Linear decrease of fluxes for conserved variables is expected for the well-mixed boundary layer below the tropical shallow cumulus (e.g., LeMone 1995). In the case of LASP/DYNAMO, the boundary layer heights observed in LASP/DYNAMO were about 600–700 m and did not seem to vary significantly except when under convection. It is a bit surprising to observe the decreasing trend of flux with increasing altitude in the non-convective cases even at below ~60-70 m, which should be in the “constant flux layer.” The negative gradient of the LHF is indicative of LHF flux convergence within the surface layer, which should result in an increase of mean water vapor in the boundary layer. Apparently, there is measurable flux divergence in the lowest levels of measurements as well. This trend of flux convergence is not visible for cases under convection. The disappearance of this trend is likely due to surface fluxes under convection being more complicated than turbulent mixing alone. The potential reason for the increased complexity is likely related to the effects of precipitation under convection. The SHF and stress profiles (Figures 19 and 20) show similar flux divergence in the lowest 70 m of the boundary layers over the Indian Ocean when there is no influence of precipitation.

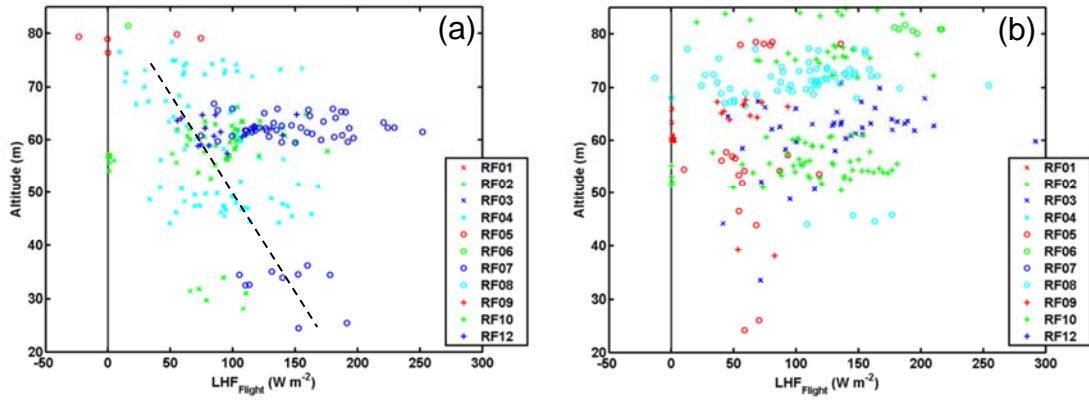


Figure 18. Latent heat flux (LHF) variation with height for (a) non-convective cases and (b) convective cases. The legend links data points with their corresponding research flight number. The dashed line is illustrative of the flux gradient in LHF.

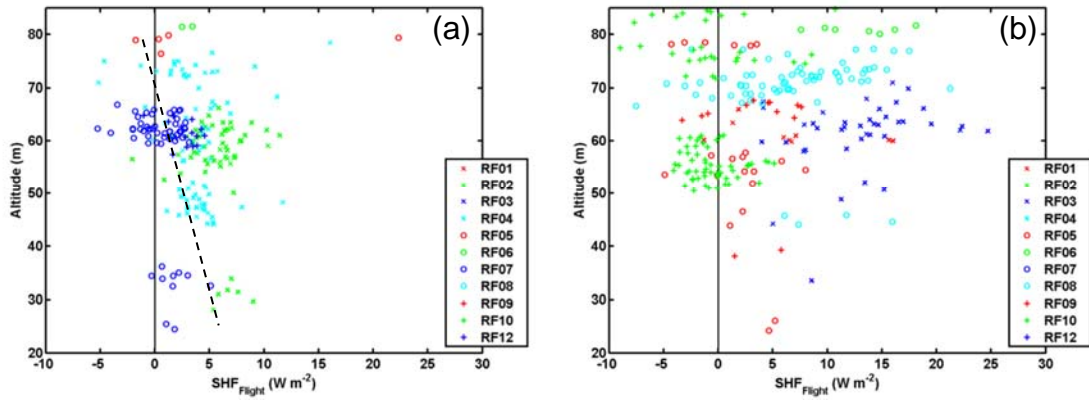


Figure 19. Same as Figure 18, except for SHF.

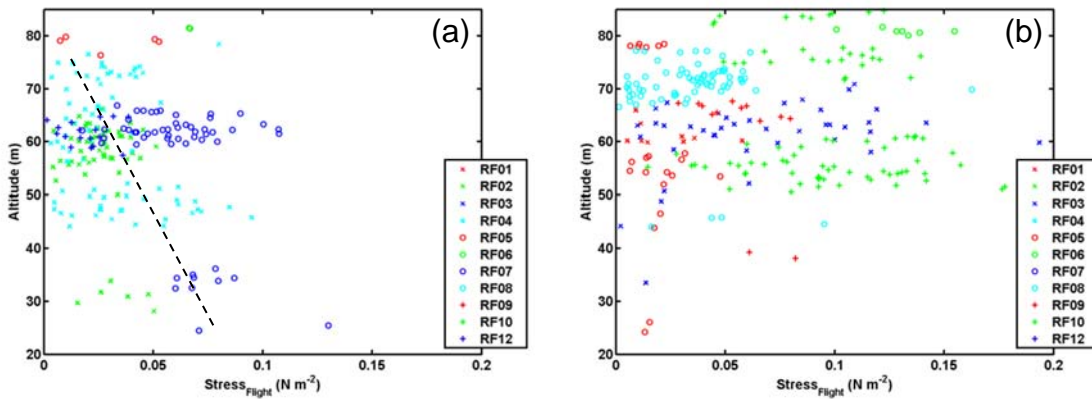


Figure 20. Same as Figure 18, except for stress.

Figures 21–23 show the variability of the fluxes with air-sea temperature difference (ASTD) as a proxy for thermal stability. The more the SST exceeds the air temperature the greater the potential for instability. When comparing the non-convective cases (panel (a) for the respective figures) with the convective cases (panel (b) for the respective figures), noticeable trends become apparent. First, nearly all measurements were made under unstable conditions with negative ASTD values. The ASTD reaches near 5 °C in the convective cases whereas the ASTD in the non-convective cases was never above 3 °C. This indicates that the convective cases have stronger thermal stability (more unstable) compared to the non-convective cases. Secondly, greater ASTD in the convective cases could be indicative of cold pools as a 2 °C drop can be obtained as a result of the cold pools associated with precipitation evaporation under the precipitating clouds. In all cases convection tends to increase the scatter in LHF, SHF, and stress as seen previously.

Figure 21 shows decreasing LHF with increasing instability for the non-convective cases, which is the opposite trend compared to SHF (Figure 22) and stress (Figure 23). The increasing magnitude of SHF with ASTD is expected based on surface layer similarity theory, while the decrease of stress with ASTD is consistent with free convection reducing low-level wind shear. The decrease of LHF with ASTD is perhaps misleading in this case as the effect of wind speed is not separated out. The large magnitude of LHF is mostly from RF07 on November 26, 2011 with strong westerly wind after the onset of the November 2011 MJO (Figure 24 to be discussed next). The strong wind resulted in significant moisture flux and the near-neutral thermal stability.

No clear correlations exist between the observed fluxes and the ASTD in the convective cases with the exception of SHF. Clearly, the LHF and stress in these cases are detached with the near-surface thermal stability because of the addition of evaporation process in the lower boundary layers.

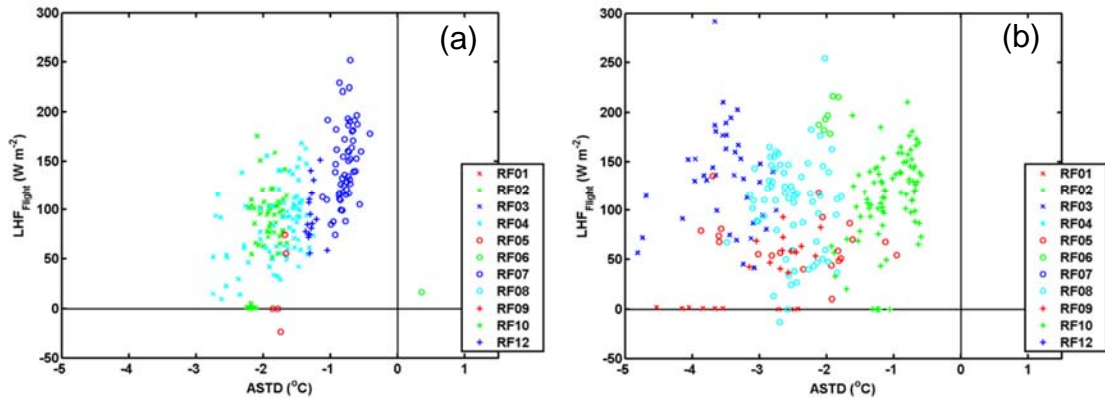


Figure 21. Variability of LHF with ASTD while (a) not under convection and (b) under convection. The legend shows the corresponding flight numbers.

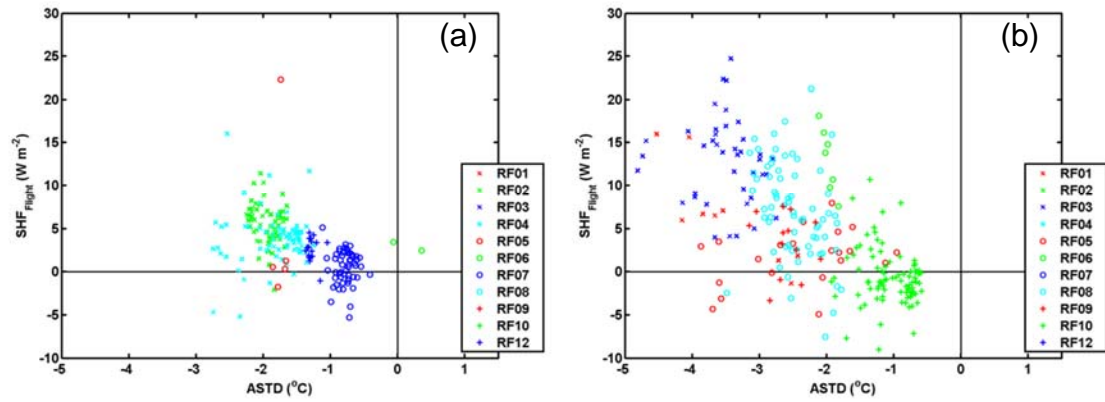


Figure 22. Same as Figure 21, except for SHF.

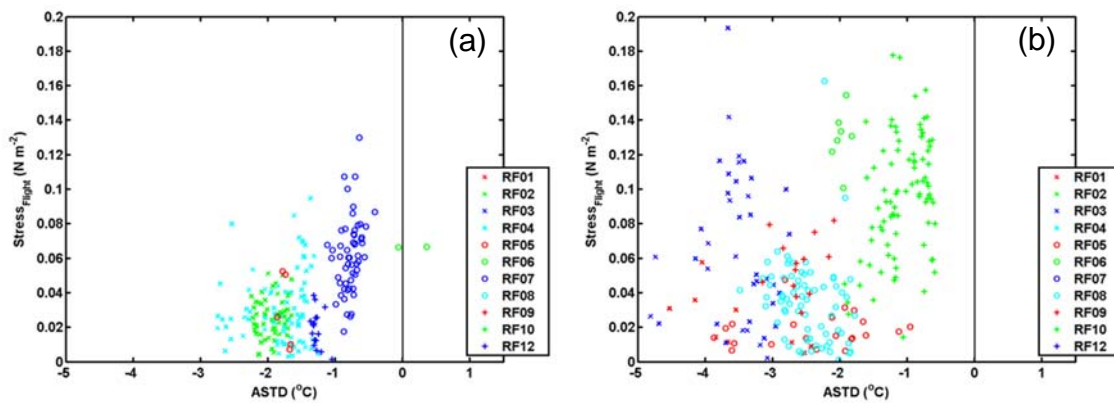


Figure 23. Same as Figure 21, except for stress.

The variation of surface fluxes with horizontal wind speed is another factor one needs to examine (Figures 24–26). The range of horizontal wind speeds was 2 m s^{-1} greater for convective cases when compared to non-convective cases. Horizontal wind speeds for non-convective cases ranged from $0\text{--}10 \text{ m s}^{-1}$ while speeds for convective cases ranged from $0\text{--}12 \text{ m s}^{-1}$. LHF maintains the same trend between non-convective (Figure 24a) and convective (Figure 24b) cases; however the scatter in the convective case is much greater. In the convective case observe a larger number of low LHF at higher wind speeds when compared to the non-convective case. Trends for SHF are not clearly maintained between the non-convective (Figure 25a) and convective (Figure 25b) cases. The variation and scatter under convective conditions is large compared to the non-convective case. Stress shows the clearest trend of increasing with horizontal wind speed. This is expected because of the nonlinear relationship between stress and wind speed as depicted by MOST.

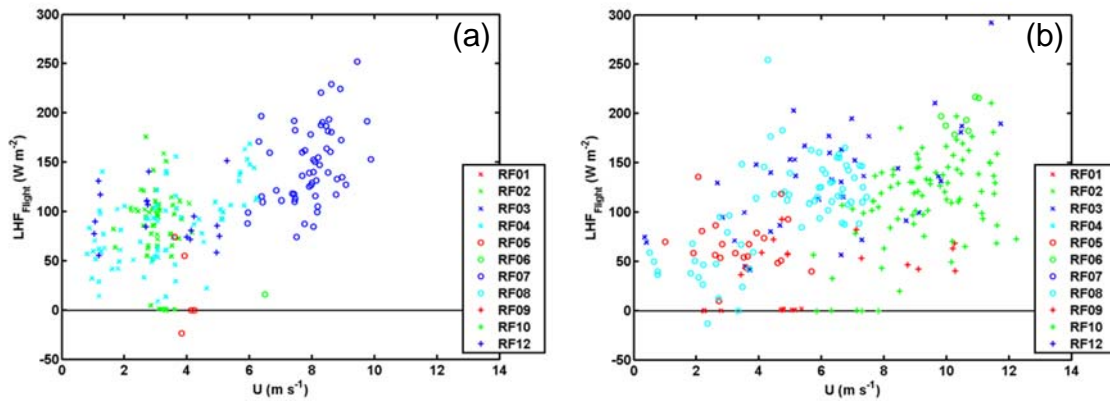


Figure 24. Variation of LHF with mean wind speed while (a) not under convection and (b) under convection.

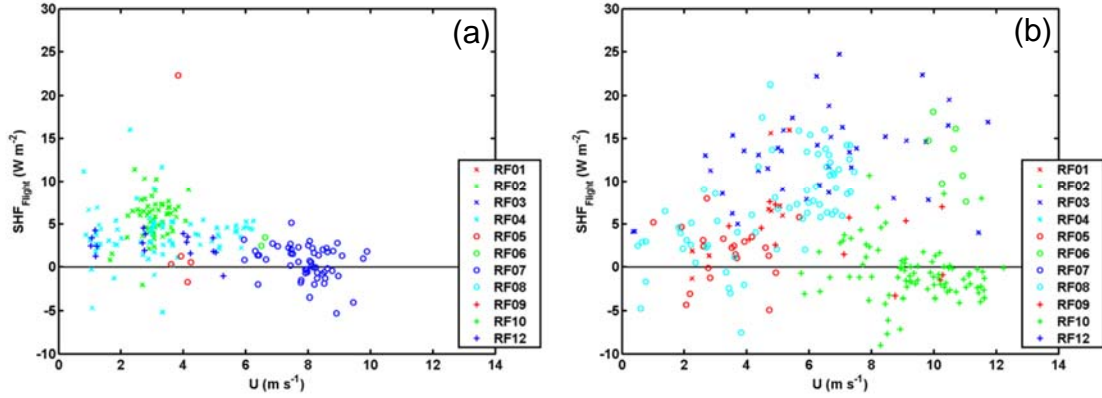


Figure 25. Same as Figure 24, except for SHF.

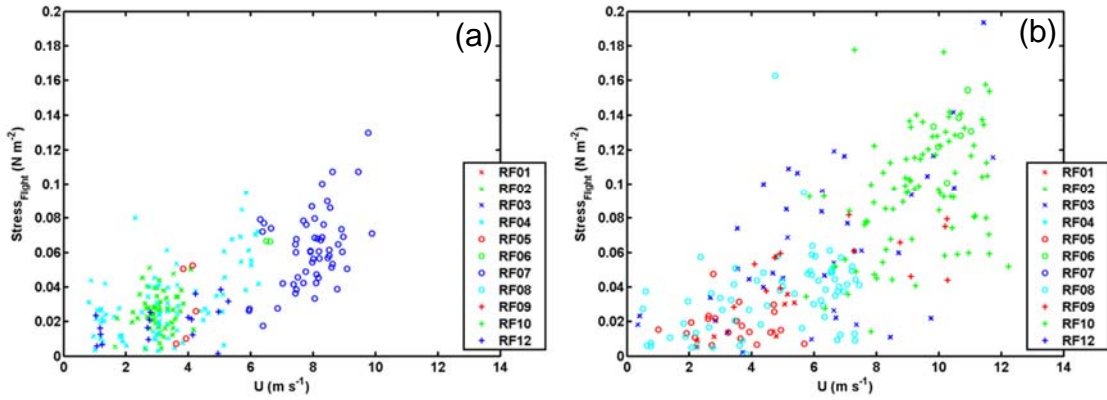


Figure 26. Same as Figure 24, except for stress.

G. SPECTRAL CHARACTERISTICS OF TURBULENCE

The spectral decomposition of surface fluxes is important in determining the dominant length scales that contribute to fluxes. This section will show a case study using LL1 of RF08. RF08 LL1 is oriented from north to south at approximately 60 m above sea level (Figure 11). The first half of the LL was under convection while the second half of the LL was not. Figures 27–30 show the time series of turbulent fluxes, thermodynamic variables, and wind components for this leg. Each time series is divided into convective and non-convective segments based on the presence of convection and possibly precipitation on the first half of the LL. The presence of convection is confirmed on the first half of LL1 in the temperature panel (Figure 28). The green line

represents the upward looking radiometric or “sky” temperature. Spikes in the sky temperature indicate the presence of low-level clouds above. Observe in each time series the increased variability under convection coinciding with the spikes in sky temperature. Figure 27 shows that the fluxes are extremely variable with large positive and negative values within the convective portion of the LL. We further analyzed this segment of data to understand the cause of the extreme flux values.

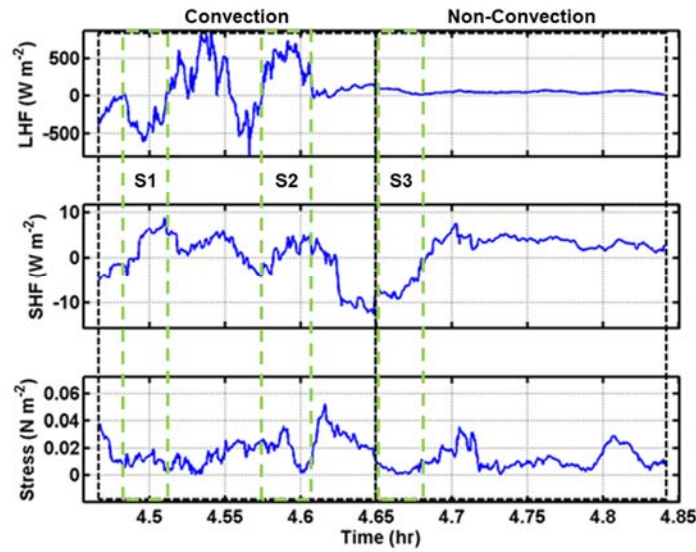


Figure 27. Time series of latent heat flux, sensible heat flux, and stress for RF08 LL1. First half of the LL is under convection and second half of the LL is not. The green dashed boxes define three special data segments (S1, S2, S3) to be discussed later in this section. Time is in UTC.

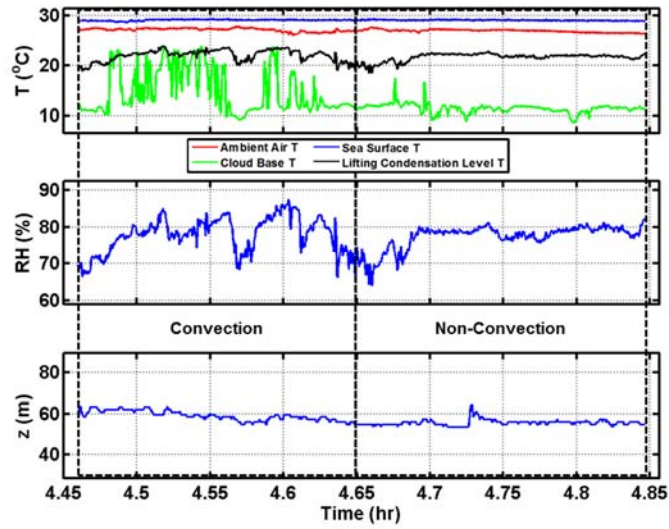


Figure 28. Time series of several temperature-related variables (see legend), relative humidity, and altitude for RF08 LL1. Regions of convection and non-convection match those in Figure 27. Time is in UTC.

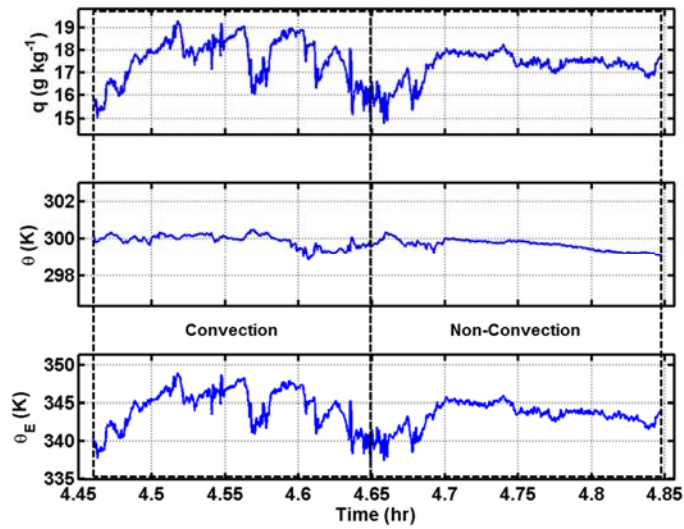


Figure 29. Time series of water vapor, potential temperature, and equivalent potential temperature for RF08 LL1. Regions of convection and non-convection match those in Figure 27. Time is in UTC.

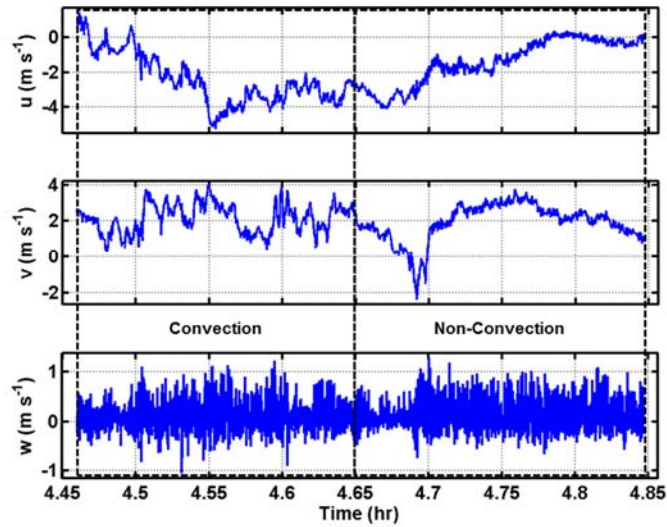


Figure 30. Time series of horizontal (u , v) and vertical (w) component velocities for RF08 LL1. Regions of convection and non-convection match those in Figure 27. Time is in UTC.

The variability of vertical velocity, temperature, and water vapor occur at different length scales. For RF08 LL1, vertical velocity shows significant mesoscale variability between non-convective (Figure 31a) and convective conditions (Figure 31b). Despite this mesoscale variability we observe similar turbulent variability with slope matching the $-5/3$ law for the spectra in the turbulence inertial subrange. The power spectra for potential temperature and water vapor in the convection conditions show much greater energy, particularly for water vapor, under convection (Figure 32b and 33b) compared to non-convection (Figure 32a and 33a). This is consistent with the increased variability seen in the time series plots in the convective segment of the RF08 LL1 (Figures 27–30).

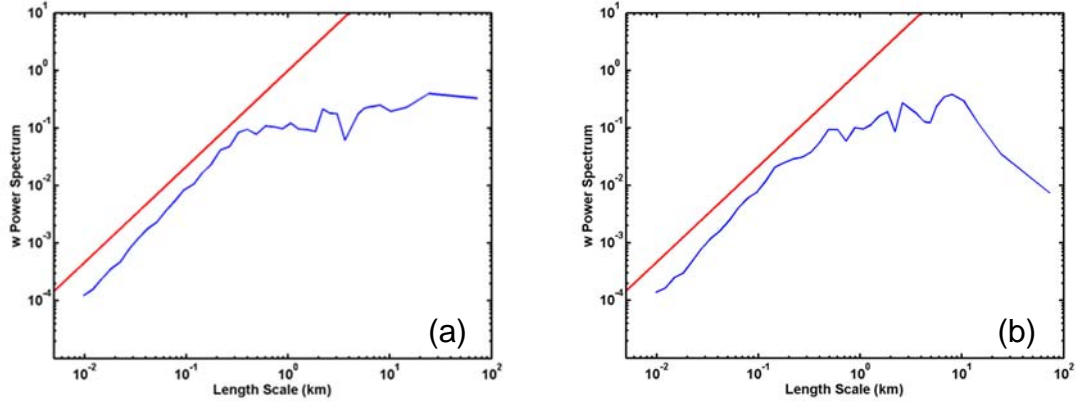


Figure 31. Power spectra of vertical velocity of (a) the non-convective segment, and (b) the convective segment of RF08 LL1. The red lines indicate the $-5/3$ slope for the turbulence inertial subrange.

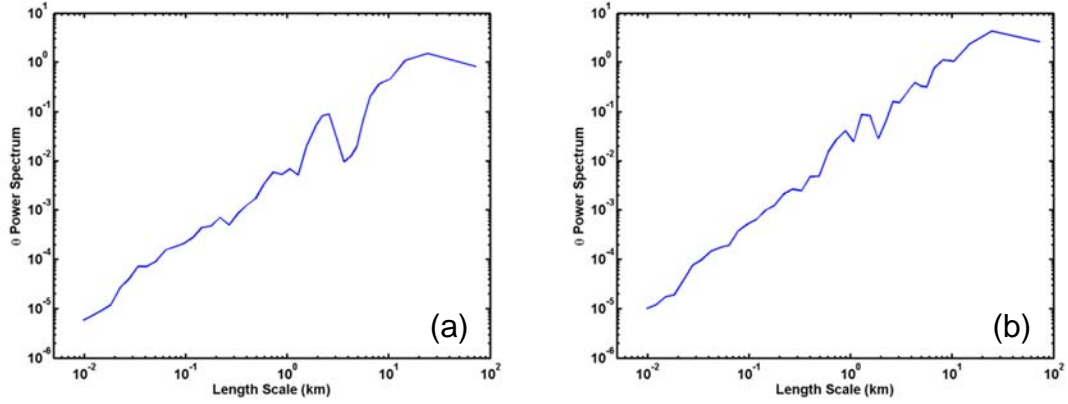


Figure 32. Same as Figure 31, except for potential temperature.

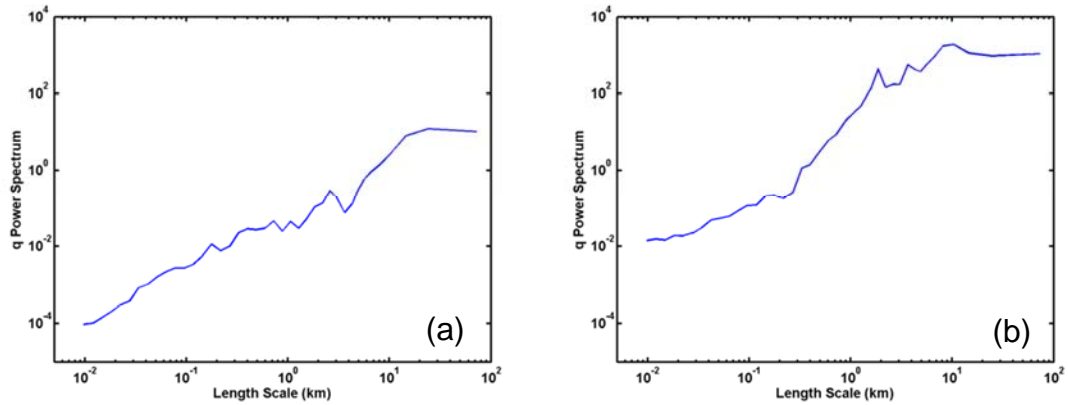


Figure 33. Same as Figure 31, except for water vapor.

The turbulence co-spectra indicate the contributions from different spatial scales to the total fluxes. Figure 34 shows the co-spectra as a function of horizontal length scale between vertical velocity and water vapor specific humidity from LL1 of RF08. The length scales greater than 1 km can be considered mesoscale, those below will be referred to as turbulence scale. For the non-convective case the co-spectra of w and q (Figure 34a) as well as the co-spectra w and θ (Figure 35a) show small positive contributions in the turbulence region for both LHF and SHF. In contrast, the co-spectra for the convective case oscillate around zero providing no clear contribution at any scale. The differences in co-spectra indicate that convection clearly introduces variability to the mesoscale and de-correlates variables in the turbulence scale (Figures 34b and 35b).

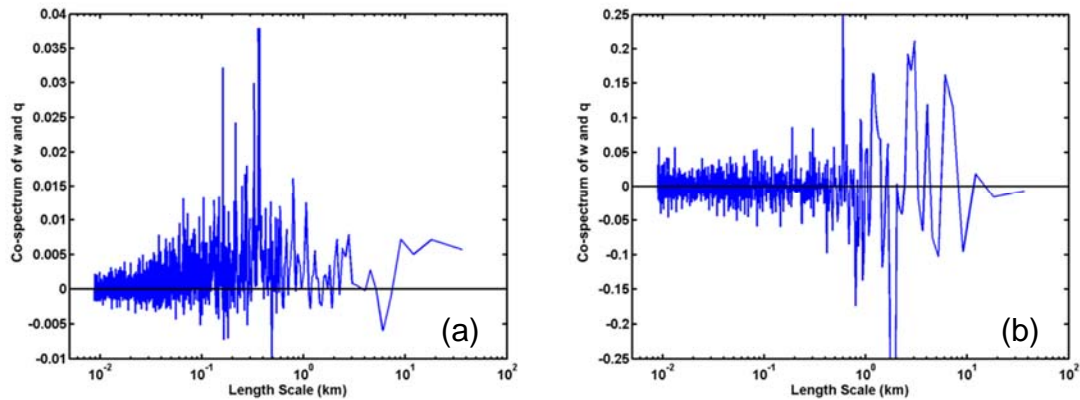


Figure 34. Vertical velocity and water vapor co-spectra of (a) the non-convective segment; and (b) the convective segment of RF08 LL1.

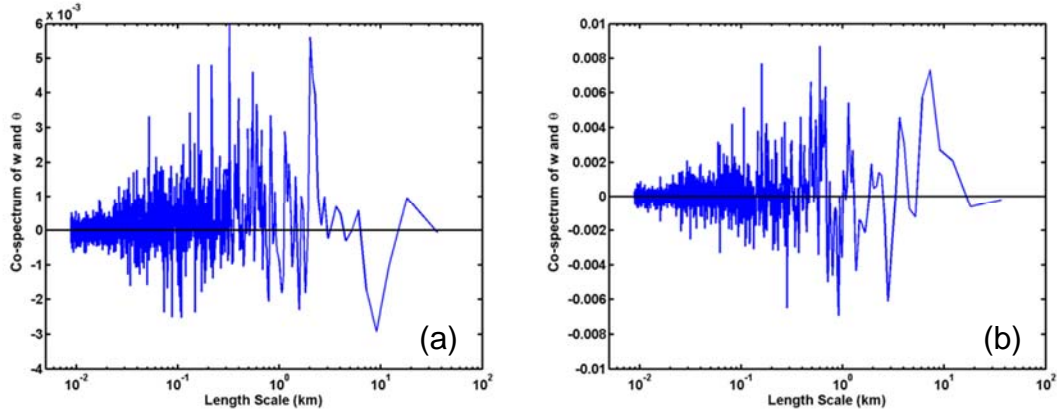


Figure 35. Same as Figure 34, except for vertical velocity and potential temperature.

In the following discussions, we will examine a few special data segments in LL1 of RF08 labeled by the green dashed boxes in Figure 27. In the convective region we will examine a region of negative LHF (S1) and a region of positive LHF (S2). A third data segment is at the transition from the convective region to the non-convective region (S3). This analysis intends to explore the cause of the extreme values of fluxes and the processes at the convection transition region through spectral analyses (Figures 36 and 37).

Figure 36 shows the power spectra of vertical velocity in the three data segments. Segments S1 and S2 show similar levels of kinetic energy in the turbulence scales. In S1, the dominant scales of variability are those greater than about 4 km. In S2, however, smaller scales of less than 2 km contribute to the kinetic energy the most. Comparing both cases in the convective region to the suppressed vertical velocities in the transition region, decreased magnitudes of the vertical velocity power spectra are observed for all length scales (Figure 36c).

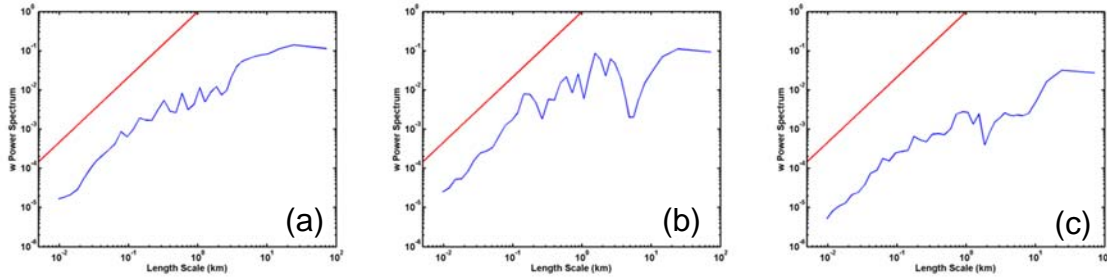


Figure 36. Vertical velocity power spectrum for RF08 LL1 (a) S1, (b) S2, and (c) S3. Red lines indicate the $-5/3$ slope for the turbulence inertial subrange.

The differences seen in the power spectra for vertical velocity are seen in the co-spectra for vertical velocity and water vapor as well as vertical velocity and potential temperature (Figures 38 and 39). In the co-spectra of vertical velocity and water vapor we see no organized flux transport under convection for S1 (Figure 38a) and S2 (Figure 38b) in all the resolvable length scales where some of the significant flux contributions at kilometer scales appear to be random. S3 (Figure 38c) co-spectrum indicates small positive transport despite the suppressed vertical velocity. The same trends are also apparent in the vertical velocity and potential temperature co-spectra (Figure 39). S1 (Figure 39a) and S2 (Figure 39b) again do not contain organized transport. It is clear that the presence of precipitation introduces processes at all scales including small scale turbulence. In contrast, S3 (Figure 44c), the transition region without the influence of precipitation, retains the most organized transport in the most chaotic, 500 m to 1000 m, length scales of S1 and S2. Because of the suppressed turbulence, the overall flux contribution in the transition region is small.

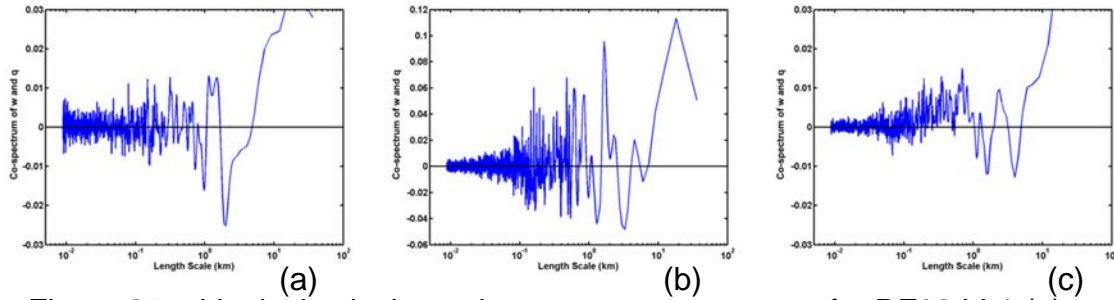


Figure 37. Vertical velocity and water vapor co-spectra for RF08 LL1 (a) S1, (b) S2, and (c) S3.

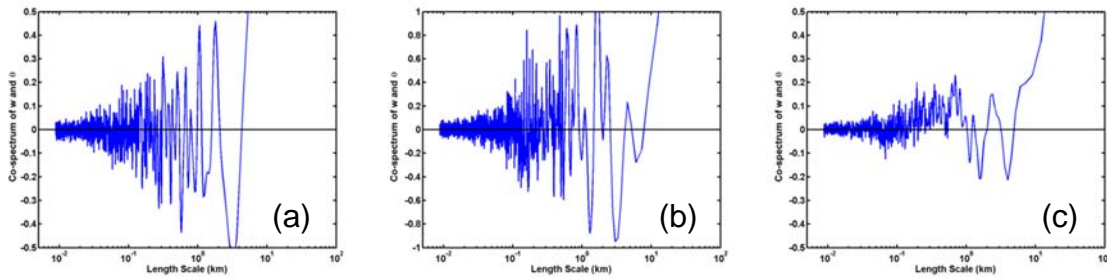


Figure 38. Same as Figure 38, except for co-spectra of vertical velocity and potential temperature.

H. VERTICAL VARIATION OF TURBULENCE

To this point we have only examined the horizontal variation of surface flux on a small altitude range close to the surface. The vertical variation of the turbulent and thermodynamic field was sampled using the FVS sampling module during RF08 in a decaying region of convection southeast of Diego Garcia. RF08 LL 17–20 compose the data set for the FVS (Figure 11). The individual fluxes calculated using eddy correlation method are displayed on Figures 39–41. On each of these figures the red line indicates LL17 at 60 m, the green line indicates LL18 at 130 m, the blue line indicates LL19 at 210 m, and the black line indicates LL20 at 310 m. The measurements of the FVS module were designed to sample each level at the same location. As a result, the data from each level are shown as distance from the same location. For comparison purposes, this method requires the assumption that the sampled features are near stationary over the period of the entire FVS.

Similar spatial variability seen at the lowest level (Figure 27) is also observed at higher levels shown in Figures 39–41, although with smaller magnitude. Horizontal variation is observed to be dominated by mesoscale variations at about 20 km wavelength. It is also seen that the LHF shows vertically coherent flux transport above the lowest level where the LHF from the top three levels are well correlated. This correlation is, nevertheless, not observed consistently in SHF and stress. It is noticed that the convection sampled by this FVS module is decaying, possibly with less precipitation compared to the active convection phase such as that sampled in RF08 LL1. Hence, the observed LHF at 60 m (LL17 in red on Figure 39) does not reach similar magnitude of variability as in the convective segment of RF08 LL1.

The SHF (Figure 40) and stress (Figure 41) consistently display a reduction in flux with increasing altitude. SHF and stress are typically, but not always greatest at the lowest sampled level. In both cases the vertical and horizontal variation are most apparent when comparing the lowest level (LL17) to any of the overhead levels.

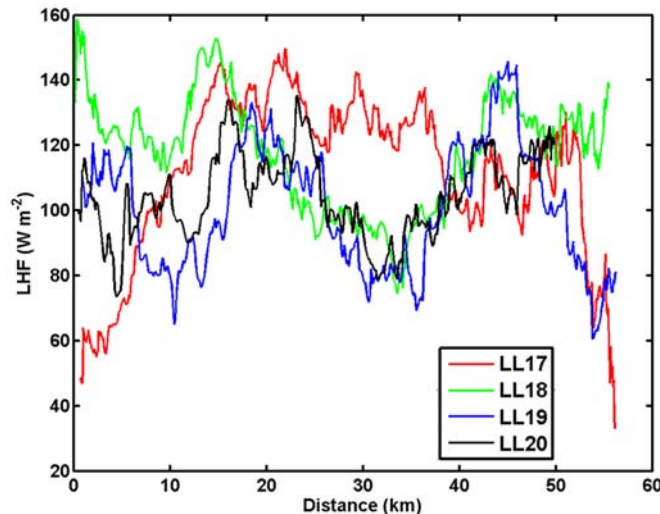


Figure 39. Horizontal variation of LHF for all legs of the RF08 FVS. Distances are from a point along the FVS line of bearing to the southwest of all four LL. LL17 is at 60 m, LL18 at 130 m, LL19 at 210 m, and LL20 at 310 m.

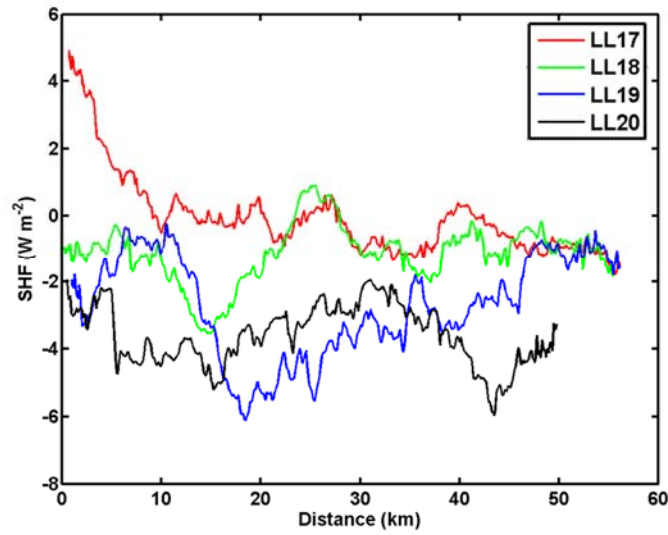


Figure 40. Same as Figure 39, except for SHF.

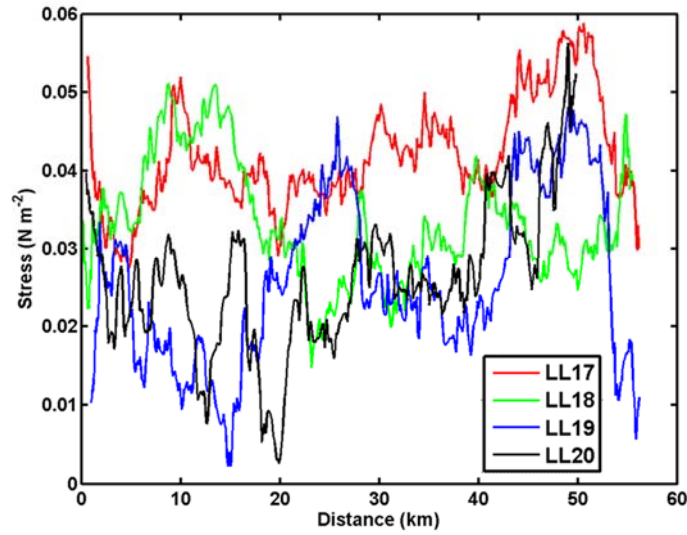


Figure 41. Same as Figure 39, except for stress.

I. EVALUATION OF COARE BULK SURFACE FLUX PARAMETERIZATION

The COARE bulk surface flux parameterization based on MOST is the most frequently used method to calculate surface fluxes in the absence of high-rate measurements that allow the use of eddy correlation method. To evaluate

the validity of COARE in parameterizing surface fluxes in different phases of the MJO over the tropical ocean, we will make a direct comparison between fluxes obtained by the COARE scheme to those obtained from the aircraft high-rate data. All measurements used here are at and below 75 m. Recall that the parameters input to COARE were averaged in the same manner and represent the same time periods as the eddy correlation method calculated fluxes. This synthesis of the data allows comparison of the state-of-the-art surface flux parameterization with the gold standard in surface flux calculation.

Figures 42a-44a provide comparisons of eddy correlation method calculated fluxes against the COARE parameterization for conditions not under convection. Figures 42b-44b provide the same comparisons for conditions under convection. The dashed lines on these figures indicate a one-to-one comparison or agreement between the calculated and the parameterized fluxes.

Figures 42–44 show that COARE in general does a good job in parameterizing the LHF and stress in this data set. For LHF, COARE provides a good representation under both non-convective (Figure 42a) and convective (Figure 42b) conditions. For non-convective cases, the general trend follows the one-to-one line, indicating no obvious bias in the parameterized fluxes. A slightly positive bias ($\sim 10 \text{ W m}^{-2}$) is seen in the parameterized LHF for convective conditions.

The parameterization of SHF is the most deficient based on this data set. In both the non-convective (Figure 43a) and convective (Figure 43b) cases the scatter mostly sits above the one-to-one line. This indicates a much greater degree of over-prediction for parameterized and measured SHF than in the case of LHF. The over-prediction for SHF under convection is most severe with a much larger bias.

The parameterized stress was highly variable compared to the measured stress. A smaller degree of variability exists for the non-convective cases (Figure 44a) when compared to the convective cases (Figure 44b). Despite the large

degree of scatter the stress in both cases balances around the one-to-one line indicating COARE tends to capture the general trends for stress.

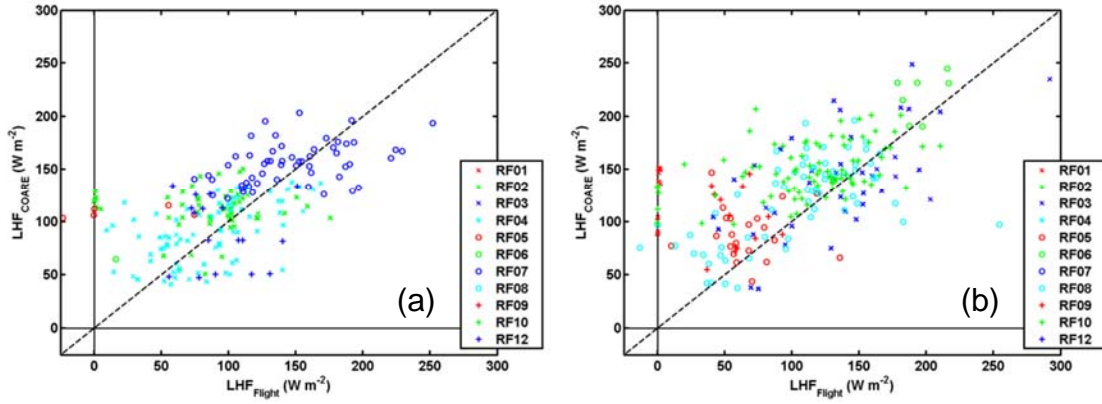


Figure 42. Convective comparison of eddy correlation method flight-measured LHF to COARE bulk surface flux parameterized LHF under (a) non-convective and (b) convective conditions. The dashed line represents a one-to-one comparison.

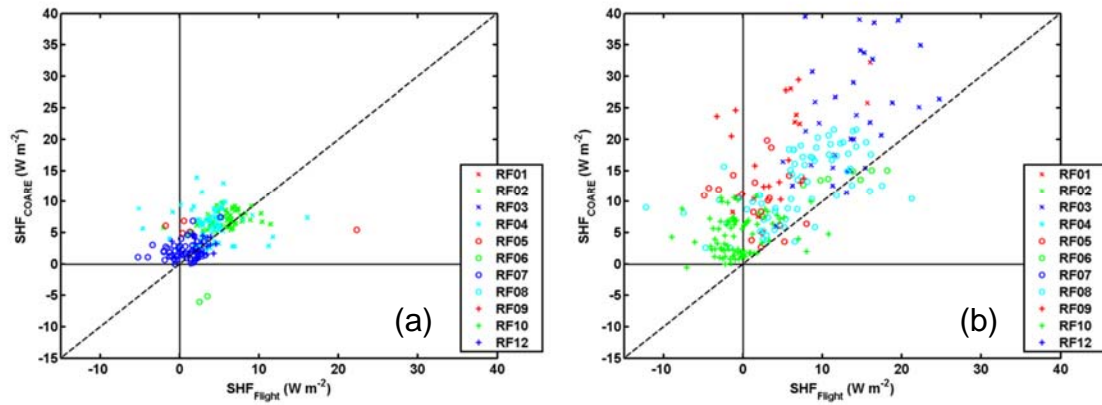


Figure 43. Same as Figure 42, except for SHF.

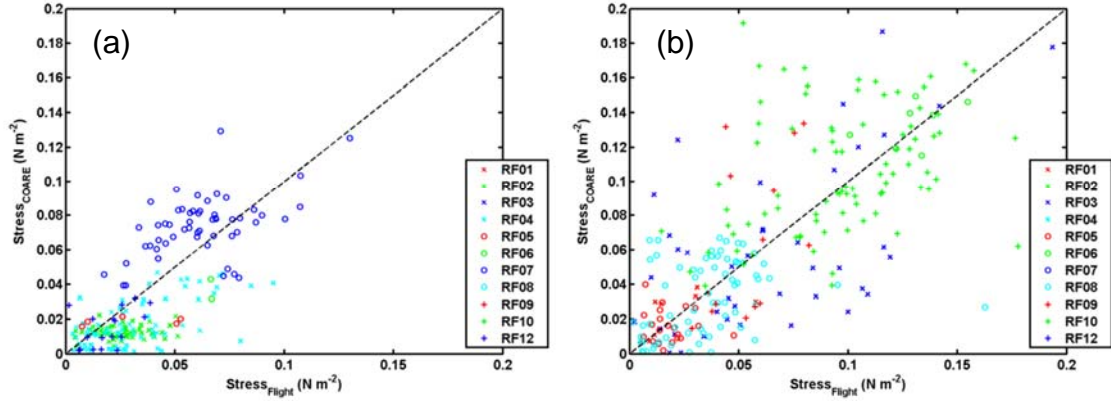


Figure 44. Same as Figure 42, except for stress.

The parameterized and measured fluxes are further compared using boxplots (Figures 45–47). For LHF, the median of the parameterized fluxes are consistently higher than the measured ones for both the non-convective (Figure 45a) and convective cases (Figure 45b). Again, the over-prediction for SHF is seen for both conditions, especially for under convection (Figure 46b) where the overestimated portion of the SHF can be larger than the magnitude of the flux itself. Stress again shows good agreement between eddy correlation method calculated flux and the COARE bulk surface flux parameterization. Overall, COARE does an acceptable job of parameterizing the observed fluxes and only deviates severely in the case of SHF under convection.

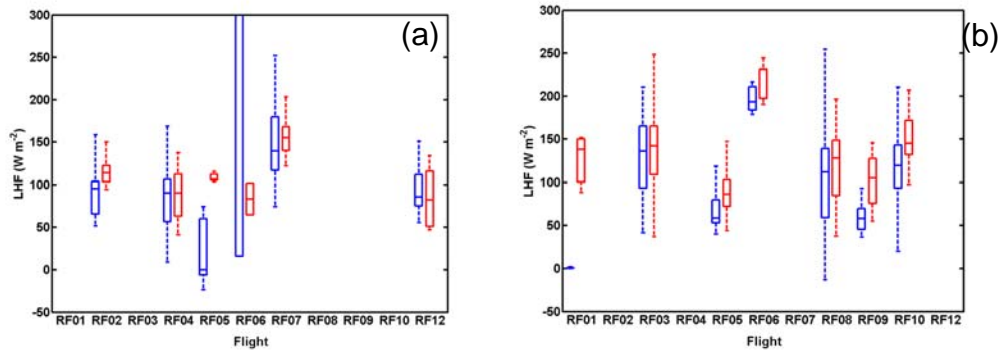


Figure 45. Boxplots comparing eddy correlation method LHF (blue) to COARE bulk surface flux parameterized LHF (red) for (a) not under convection and (b) under convection.

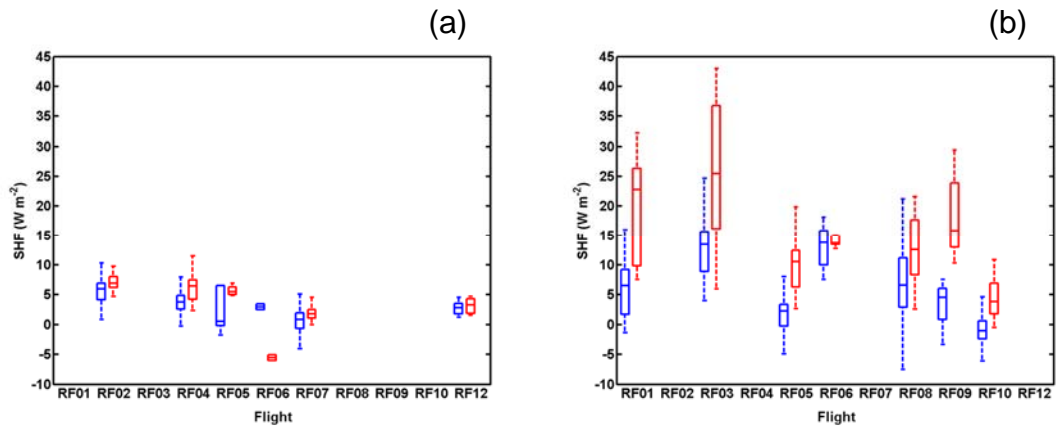


Figure 46. Same as Figure 45, except for SHF.

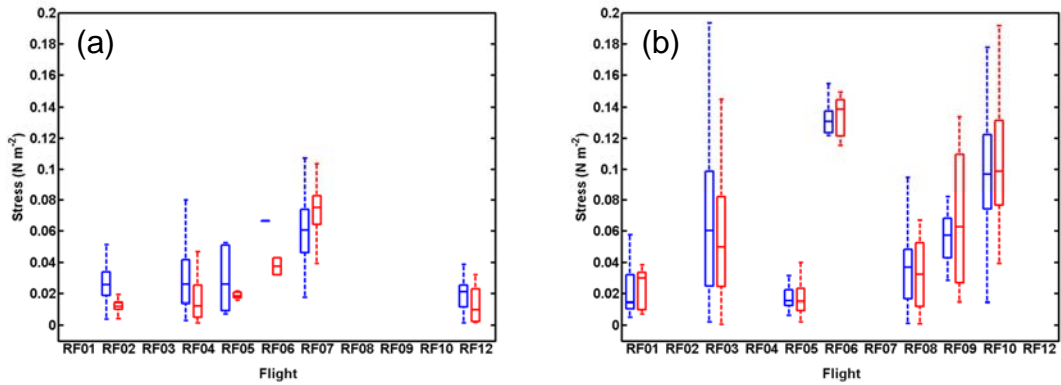


Figure 47. Same as Figure 45, except for stress.

V. CONCLUSIONS

A. SUMMARY AND CONCLUSIONS

A total number of 85 level legs below 75 m measured with the NOAA P-3 during the LASP/DYNAMO 2011 experiment were analyzed in this thesis work to examine the effects of convective precipitation on surface fluxes and surface flux parameterization. For this purpose, surface fluxes were calculated using the eddy correlation method from each of the 10 km segments of the near-surface level legs. The mean wind and thermodynamic variables are also calculated and used to estimate surface fluxes using the COARE bulk flux parameterization. The SST was corrected for radiation and water vapor errors using AXBT/AXCTD measurements, which was part of the input for the COARE parameterization.

Surface fluxes under convection and non-convection conditions show some distinctly different characteristics. Much larger variability in all three fluxes is seen in the convection cases in general. In non-convective conditions, turbulent fluxes show a clear trend of vertical convergence in all fluxes even in the lowest 75 m. The presence of the constant flux layer was thus not observed in the LASP/DYNAMO cases. Given that the boundary layer heights were between 600–700 m during the LASP/DYNAMO observation period, the majority of the identified low level LL should be within the marine atmospheric surface layer. The results in this study clearly indicate a much stronger vertical flux gradient compared with many previous studies suggesting the presence of a constant flux surface layer.

Analysis of the variability of surface fluxes under convection and not under convection focused on measurements collected on a LL partially under convection during RF08. Comparison of the convective and non-convective portions of the LL demonstrated the chaotic nature of flux under convection. Convective examples showed a high degree of variability with large magnitude positive and negative fluxes. Under convection, fluctuations in surface fluxes

were large in magnitude and demonstrated no clear contribution at any particular spatial scale. In contrast, non-convective examples experienced a small positive contribution to surface flux in the turbulence region with much smaller magnitude oscillations. The lack of clear transport in the convective case highlights that processes beyond turbulence transport are occurring under convection.

The horizontal variability of surface fluxes was also apparent under convection at multiple levels up to about 310 m above the surface using measurements from a FVS module on RF08. This thesis work suggests that the influence of the convective precipitation is beyond the lowest measurement levels even though the analyses focused on the lowest level of measurements.

The ultimate objective of this analysis was to evaluate the applicability of the state-of-the-art COARE bulk surface flux parameterization in the case of strong convection with precipitation. This is achieved by comparison of the fluxes using the gold standard in surface flux calculation, eddy correlation method, with the COARE parameterized fluxes using data from 11 of the 12 research flights in LASP/DYNAMO. This comparison was made for cases under convection and not under convection to allow for evaluation of COARE bulk surface flux parameterization performance under both conditions.

The direct comparison of eddy correlation method and COARE bulk surface fluxes further confirmed the COARE bulk surface flux parameterization as a suitable parameterization tool for surface fluxes with a few exceptions. COARE provided a good representation of LHF under non-convective conditions and a slight over-prediction by COARE was apparent for the convective cases. Sensible heat flux was over-predicted by COARE for both the convective and non-convective cases. The convective cases saw substantial over-prediction, increased scattering, and large magnitude for SHF, especially when compared to the non-convective cases. This can be explained by presence of the cold pool due to rain water evaporation under the cloud base. Together with the enhanced downdrafts, the layer under convection has colder and drier air in the convective region as depicted by cold pool forming mechanisms. Stress generally compares

well between eddy correlation method and COARE, although much larger scattering occurred under convection. Because convection introduces the evaporation process between the cloud base and the surface, the nature of flux transport is complicated and less organized compared to the non-convection cases where turbulence is the main mechanism for flux transport.

B. REMAINING ISSUES AND RECOMMENDATIONS

The use of the COARE algorithm assumes that the measurements were made in the surface layer with constant turbulent fluxes. This may not always be the case as seen in the convergence of fluxes with height in the results. Unfortunately, this study is limited by the lack of sustained aircraft measurement below 60 m due to safety considerations. This introduces some uncertainty into the COARE bulk surface flux parameterization comparisons as it remains possible that some of the data points could have been slightly above the surface layer. It is thus highly desirable for future study to use new measurement capabilities that can make flux measurements consistently within the surface layer. Accuracy of the SST continues to be an unresolved issue when attempting to evaluate surface flux parameterization, which is also a direction for further improvements.

THIS PAGE INTENTIONALLY LEFT BLANK

LIST OF REFERENCES

- Betts, A. K., 1976: The thermodynamic transformation of the tropical subcloud layer by precipitation and downdrafts. *J. Atmos. Sci.*, **33**, 1008–1020.
- Charnock, H., 1955: Wind stress on a water surface. *Quart. J. Roy. Met. Soc.*, **81**, 639–640.
- Corfidi, S. F., 2003: Cold pools and MCS propagation: Forecasting the motion of downwind-developing MCSs. *Wea. Forecasting*, **18**, 997–1017.
- Echternacht, K. L., and M. Garstang, 1976: Changes in the structure of the tropical subcloud layer from the undisturbed to disturbed states. *Mon. Wea. Rev.*, **104**, 407–417.
- Edson, J. B., C. W. Fairall, P. G. Mestayer, and S. E. Larsen, 1991: A study of the inertial-dissipation method for computing air-sea fluxes. *J. Geophys. Res.*, **96**, 10689–10711.
- Fairall, C. W., E. F. Bradley, J. S. Godfrey, G. A. Wick, J. B. Edson, and G. S. Young, 1996a: Cool-skin and warm layer effects on sea surface temperature. *J. Geophys. Res.*, **101**, 1295–1308.
- Fairall, C. W., E. F. Bradley, J. E. Hare, A. A. Grachev, and J. B. Edson, 2003: Bulk parameterization of air-sea fluxes: Updates and verification for the COARE algorithm. *J. Climate*, **16**, 571–591.
- Fairall, C. W., E. F. Bradley, D. P. Rogers, J. B. Edson, and G. S. Young, 1996b: Bulk parameterization of air-sea fluxes for tropical ocean-global atmosphere coupled-ocean atmosphere response experiment. *J. Geophys. Res.*, **101**, 3747–3764.
- Godfrey, J. S., and A. C. M. Beljaars, 1991: On the turbulent fluxes of buoyancy, heat, and moisture at the air-sea interface at low wind speeds. *J. Geophys. Res.*, **96**, 22043–22048.
- Hare, J. E., T. Hara, J. B. Edson, and J. M. Wilczak, 1997: A similarity analysis of the structure of air flow over surface waves. *J. Phys. Oceanogr.*, **27**, 1018–1037.
- Hendon, H. H., and J. Glick, 1997: Intraseasonal air-sea interaction in the tropical Indian and Pacific Oceans. *J. Climate*, **10**, 647–661.
- Jabouille, P., J. L. Redelsperger, and J. P. Lafore, 1996: Modification of surface fluxes by atmospheric convection in the TOGA COARE region. *Mon. Wea. Rev.*, **124**, 816–837.

- Jorgensen, D. P., M. A. LeMone, and S. B. Trier, 1997: Structure and evolution of the 22 February 1993 TOGA COARE squall line: Aircraft observations of precipitation, circulation, and surface energy fluxes. *J. Atmos. Sci.*, **54**, 1961–1985.
- Kalogiros, J., and Q. Wang, 2011: Aircraft observations of sea-surface turbulent fluxes near the California coast. *Boundary-Layer Meteor.*, **139**, 283–306.
- Kudryatsev, V. N., and V. K. Makin, 2004: Impact of swell on the marine atmospheric boundary-layer. *J. Phys. Oceanogr.*, **34**, 934–949.
- LeMone, M. A., 1973: The structure and dynamics of horizontal roll vortices in the planetary boundary layer. *J. Atmos. Sci.*, **30**, 1077–1091.
- LeMone, M. A., 1995: The cumulus-topped boundary layer over the ocean. *The Boundary Layer and its Parameterization*, C. H. Moeng, Ed., National Center for Atmospheric Research, 109–136.
- Lind, R. J., and W. J. Shaw, 1989: Sea surface temperature fields derived from aircraft and ship observations during FASINEX 1986. NPS-63-89-001, 41 pp.
- National Oceanic and Atmospheric Administration Air Operations Center, cited 2014: Lockheed WP-3D Orion. [Available online at http://www.aoc.noaa.gov/aircraft_lockheed.htm].
- Sullivan, P. P., J. B. Edson, T. Hristov, and J. C. McWilliams, 2008: Large-eddy simulations and observations of atmospheric marine boundary layers above nonequilibrium surface waves. *J. Atmos. Sci.*, **65**, 1225–1245.
- Thompson, D. B., and P. E. Roundy, 2013: The relationship between the Madden-Julian oscillation and U.S. violent tornado outbreaks in the spring. *Mon. Wea. Rev.*, **141**, 2087–2095.
- Tompkins, A. M., 2001: Organization of tropical convection in low vertical wind shears: The role of cold pools. *J. Atmos. Sci.*, **58**, 1650–1672.
- Vickers, D., and S. K. Esbensen, 1998: Subgrid surface fluxes in fair weather conditions during TOGA COARE: Observational estimates and parameterization. *Mon. Wea. Rev.*, **126**, 620–633.
- Wang, Y., and B. Geerts, 2010: Humidity variations across the edge of trade wind cumuli: Observations and dynamical implications. *Atmos. Res.*, **97**, 144–156.
- Wang, Y., B. Geerts, and J. French, 2009: Dynamics of the cumulus cloud margin: An observational study. *J. Atmos. Sci.*, **66**, 3660–3677.

- Wang , Q., D. Khelif, D. Jorgensen, A. Bucholtz, C. Zappa, and P. Chuang, cited 2013: P-3 Mission Summary. [Available online at http://met.nps.edu/~qwang/DYNAMO/DYNAMO_P3_Mission_Summary.pdf].
- Young, G. S., S. M. Perugini, and C. W. Fairall, 1995: Convective wakes in the equatorial western Pacific during TOGA. *Mon. Wea. Rev.*, **123**, 110–123.
- Zhang, C., 2005: Madden-Julian Oscillation, *Rev. Geophys.*, **43**, 1–36.
- Zuidema, P., Z. Li, R. J. Hill, L. Bariteau, B. Rilling, C. Fairall, W. A. Brewer, B. Albrecht, and J. Hare, 2012: On trade wind cumulus cold pools. *J. Atmos. Sci.*, **69**, 258–280.

THIS PAGE INTENTIONALLY LEFT BLANK

INITIAL DISTRIBUTION LIST

1. Defense Technical Information Center
Ft. Belvoir, Virginia
2. Dudley Knox Library
Naval Postgraduate School
Monterey, California